

Low seismic velocities below mid-ocean ridges: Attenuation versus melt retention

Saskia Goes,¹ John Armitage,² Nick Harmon,³ Hannah Smith,^{1,4} and Ritske Huismans⁵

Received 18 July 2012; revised 8 October 2012; accepted 11 October 2012; published 14 December 2012.

[1] The first comprehensive seismic experiment sampling subridge mantle revealed a pronounced low-velocity zone between 40 and 100 km depth below the East Pacific Rise (EPR) that has been attributed to substantial retained melt fractions of 0.3–2%. Such high melt fractions are at odds with low melt productivity and high melt mobility inferred from petrology and geochemistry. Here, we evaluate whether seismic attenuation can reconcile subridge seismic structure with low melt fractions. We start from a dynamic spreading model which includes melt generation and migration and is converted into seismic structure, accounting for temperature-, pressure-, composition-, phase-, and melt-dependent anharmonicity, and temperature-, pressure-, frequency- and hydration-dependent anelasticity. Our models predict a double low-velocity zone: a shallow—approximately triangular—region due to dry melting, and a low-velocity channel between 60 and 150 km depth dominantly controlled by solid state high-temperature seismic attenuation in a damp mantle, with only a minor contribution of (<0.1%) melt. We test how tomographic inversion influences the imaging of our modeled shear velocity features. The EPR experiment revealed a double low-velocity zone, but most tomographic studies would only resolve the deeper velocity minimum. Experimentally constrained anelasticity formulations produce V_S as low as observed and can explain lateral variations in near-ridge asthenospheric V_S with ± 100 K temperature variations and/or zero to high water content. Furthermore, such Q_S formulations also reproduce low asthenospheric V_S below older oceans and continents from basic lithospheric cooling models. Although these structures are compatible with global Q_S images, they are more attenuating than permitted by EPR data.

Citation: Goes, S., J. Armitage, N. Harmon, H. Smith, and R. Huismans (2012), Low seismic velocities below mid-ocean ridges: Attenuation versus melt retention, *J. Geophys. Res.*, 117, B12403, doi:10.1029/2012JB009637.

1. Introduction

[2] Plate creation at mid-ocean ridges is often regarded as the simplest and best understood of plate tectonic processes, involving decompression melting of passively rising mantle material, in response to spreading of the plates. However, the few regional seismic images of the mantle below a ridge reveal surprising complexity. The MELT experiment across a section of the East Pacific Rise (EPR) confirmed there was no deep-seated source of hot material below the ridge, as expected for passive upwelling [Forsyth *et al.*, 1998]. However, the combined data from the MELT and GLIMPSE experiments along

the southern EPR, and data from an experiment in the Gulf of California revealed three-dimensional mantle velocity anomalies that are often not centered below the ridge [Forsyth *et al.*, 1998; Gu *et al.*, 2005; Harmon *et al.*, 2011; Wang *et al.*, 2009; Weeraratne *et al.*, 2007]. The three dimensionality has been proposed to reflect a dynamic component of mantle upwelling and possibly also downwelling caused by and/or causing along- and across-strike variations in temperature, composition and melt concentrations [Harmon *et al.*, 2011; Katz, 2010; Toomey *et al.*, 2002; Wang *et al.*, 2009].

[3] Equally surprising about the images was the strength of low-velocity anomalies between 50 and 150 km depth. These appear to require substantial melt retention at fractions of 0.3–2% [Forsyth *et al.*, 1998; Harmon *et al.*, 2009; Yang *et al.*, 2007]. Such high melt concentrations at depth are at odds with the understanding of melt transport from the decay of Ra, Pa and Th [e.g., Lundstrom, 2003; Rubin *et al.*, 2005; Stracke *et al.*, 2006] and estimates of grain size [Behn *et al.*, 2009] and its effect on melt permeability [Connolly *et al.*, 2009; Faul, 2001] unless these images are capturing the melt migration in flux.

[4] The contribution of melt to the properties of asthenosphere in general has long been debated. However, a broad

¹Department of Earth Science and Engineering, Imperial College London, London, UK.

²IPG Paris, Paris, France.

³NOC Southampton, Southampton, UK.

⁴Now at Al Sadiq and Al Zahra School, London, UK.

⁵Department of Earth Science, University of Bergen, Bergen, Norway.

Corresponding author: S. Goes, Department of Earth Science and Engineering, Imperial College London, London SW7 2AZ, UK. (s.goes@imperial.ac.uk)

©2012. American Geophysical Union. All Rights Reserved.
0148-0227/12/2012JB009637

range of studies has shown that the asthenospheric low-velocity zone under continents and oceans can be explained purely thermally, without any requirement for significant fractions of melt, by accounting for anelastic effects on wave propagation as constrained by laboratory-derived anelasticity parameters [Faul and Jackson, 2005; Goes et al., 2000; Karato, 2012; Karato and Jung, 1998; Priestley and McKenzie, 2006; Röhm et al., 2000; Shapiro and Ritzwoller, 2004b; Sheehan and Solomon, 1992; Stixrude and Lithgow-Bertelloni, 2005]. Such an interpretation is consistent with petrological constraints that predict low melt productivity at asthenospheric depths, where melting has to be volatile assisted, and predict that melt is efficiently removed [Asimow et al., 2004; Hirschmann, 2010]. So, there is no strong evidence for substantial accumulations of melt in most of the oceanic asthenosphere, although the detection of a widespread seismic ‘LAB’ discontinuity, where velocity decreases with depth by as much as several percent, has revived discussion about accumulations of a thin layer of melt below a compositional or rheological boundary at the base of the lithosphere [e.g., Kawakatsu et al., 2009; Rychert and Shearer, 2009]. Alternatively, it has been proposed that dehydration together with a change in dominant anelastic deformation mechanism may explain this discontinuity without requiring substantial amounts of melt [Karato, 2012].

[5] Here we explore to what extent the very low velocities in the mantle below mid-ocean ridges can be explained by intrinsic high-temperature attenuation without the need for larger amounts of retained melt than expected from petrological and geochemical constraints. Previous studies have qualitatively compared dynamic models predicting the geometry of the subridge melt region with seismic images from the MELT experiment [Conder et al., 2002; Katz, 2010; Toomey et al., 2002] and have proposed possible causes for the asymmetry of the mantle structure. A few studies performed more quantitative comparisons between imaged velocities and those predicted from oceanic cooling models without melt [Harmon et al., 2009; Yang et al., 2007], and concluded that the presence of melt was required to match the seismic constraints. In this study, we make a self-consistent forward model of subridge temperature, melt generation and melt migration that uses an established modeling approach, similar to several previous studies [Braun et al., 2000; Conder et al., 2002; Toomey et al., 2002]. We convert the geodynamic models into seismic structure taking into account the effects of phase, anelastic attenuation and the presence of melt, considering a range of anelasticity formulations. Finally, we do a more rigorous comparison between the synthetic models and seismically imaged structure by performing a set of resolution tests for the data distribution of the EPR experiments.

2. Subridge Seismic Constraints

[6] Analyses of seismic structure below the oceans consistently find an asthenospheric low-velocity zone that deepens and increases in shear speed with age [Kustowski et al., 2008; Maggi et al., 2006; Nishimura and Forsyth, 1989; Ritzwoller et al., 2004; Shapiro and Ritzwoller, 2002]. Such structure is predominantly constrained by surface waves with periods in the range 15–160 s, which are the data with the best sensitivity to amplitude and depth distribution of shallow mantle velocities. Global or ocean-wide seismic models find minimum isotropic shear velocities below ridges of around 4.1 km/s

between 50 and 100 km depth. The low-velocity zone deepens to 125–175 km depth for 120 Ma old oceanic lithosphere, with a minimum isotropic V_S of around 4.4 km/s. Another consistently found characteristic of shallow oceanic mantle structure is a radial anisotropy down to about 250 km depth. Below oceanic lithosphere, V_{SH} generally exceeds V_{SV} by 0.1–0.2 km/s [Kustowski et al., 2008; Nishimura and Forsyth, 1989; Shapiro and Ritzwoller, 2002], a pattern expected for predominant horizontal flow [Becker et al., 2008].

[7] The regional models derived from the surface waves recorded by the MELT and GLIMPSE experiments recover a strong shallow low-velocity anomaly down to about 50 km with an amplitude of over 11%, peaking at around 10 km depth offset slightly westward from the ridge [Dunn and Forsyth, 2003]. They also reveal a deeper low-velocity anomaly between about 50 and 100 km depth with minimum velocities similar to those found in the ocean-scale models: 3.9 (V_{SV}) to 4.15 (V_{SH}) [Dunn and Forsyth, 2003; Harmon et al., 2009, 2011], but offset about 150 km west of the ridge (Figure 1). Some 1-D average models [Gu et al., 2005; Webb and Forsyth, 1998] find even lower V_{SV} , down to 3.7–3.8 km/s between 50 and 100 km depth for southern EPR along-ridge paths. These may reflect along-ridge variations in velocity structure, but may also be biased low by focusing and multipathing; that is, the low velocities at the ridge may act as a waveguide and focus energy [e.g., Dunn and Forsyth, 2003]. Immediately east of the EPR, the deeper low-velocity zone appears to deepen (data coverage do not extend beyond about 200 km from the ridge), and minimum velocities are about 0.1–0.15 km/s higher than to the west [Dunn and Forsyth, 2003; Harmon et al., 2009, 2011]. A more recent experiment across the young oceanic ridge in the Gulf of California [Wang et al., 2009] reveals a velocity minimum between 40 and 70 km depth of similar amplitude as below the EPR ($V_{SV} = 4.05 \pm 0.05$ km/s) and minima that are not aligned with the surface trace of the ridge.

[8] Global- and ocean-scale models display a clear correlation between oceanic cooling age and attenuation [e.g., Dalton et al., 2008, 2009; Sheehan and Solomon, 1992]. The most recent global shear attenuation model with corrections for the effects of scattering [Dalton et al., 2008], finds minimum Q_S values below ridges of 40–70, compared with a value of around 80 in global 1-D attenuation models like PREM [Dziewonski and Anderson, 1981]. These numbers are in line with earlier studies that estimated asthenospheric Q_S below young lithosphere in the range of 50 [e.g., Sheehan and Solomon, 1992]. Several other studies have found Q_S values below ridges that are at least 50% lower than PREM’s asthenospheric value [Bhattacharyya et al., 1996; Billien et al., 2000; Gung and Romanowicz, 2004]. All these studies used long-period waves (in the range 10–150 s), and assumed frequency-independent Q_S . The global-scale models only resolve large-scale (on the order of 1000 km) anomalies. Given the large and rapid variations in Q_S expected from its exponential dependence on temperature, they most likely underestimate the amplitude of Q variations. Indeed, more regional studies of attenuation indicate larger variability [Mitchell, 1995]. For example, under the Basin and Range, where asthenospheric V_S is as low as below the ridges, Q_S values as low as 20 have been inferred [Hwang et al., 2009].

[9] The single available regional mid-ocean ridge Q_S model, derived from analysis of the GLIMPSE and MELT

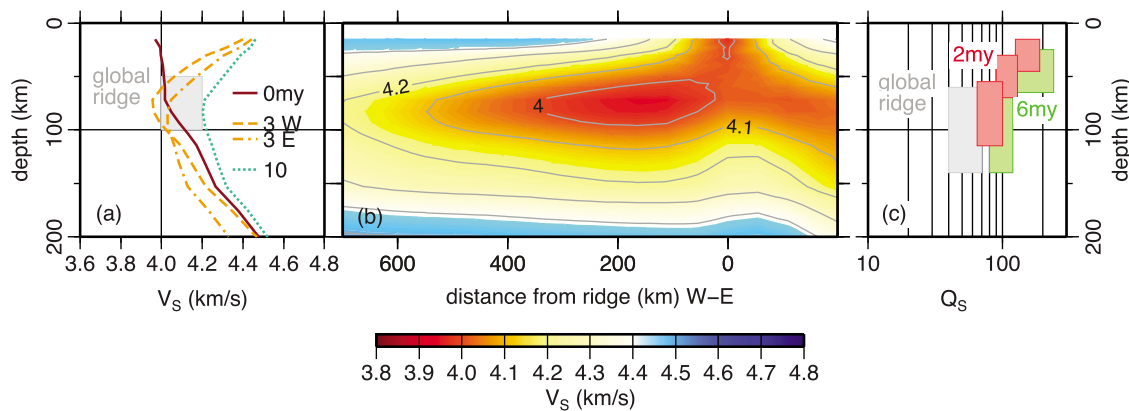


Figure 1. Regional East Pacific Rise (EPR) and global seismic constraints of subridge structure. (a and b) The 2-D V_{SV} model as a function of age across the EPR from the joint MELT and GLIMPSE data by *Harmon et al.* [2009] (polynomial parameterization), as profiles at various ages both west and east of the ridge (Figure 1a) and in cross section (Figure 1b). Spreading velocity is 7.2 cm/yr; that is, 3 Myr ('3W', '3E') profiles are located 216 km from the ridge axis, 10 Myr ('10') profile at 720 km. (c) The shear attenuation structure inferred from the same EPR data set by *Yang et al.* [2007] for two age ranges. For comparison, the gray boxes in Figures 1a and 1c show the range of minimum mantle (isotropic) V_S , and minimum Q_S , respectively, below mid-ocean ridges from global models (references in the main text).

data, disagrees with the ocean-wide Q_S models. *Yang et al.* [2007] simultaneously inverted fundamental mode Rayleigh wave amplitude and phase data (16–67 s) for phase velocities and attenuation coefficients. In their inversion, they used 2-D finite frequency sensitivity kernels, which correct for the effects of single scattering on amplitude loss. In addition, they accounted for variations in amplitude caused by the incoming wavefield using a 2-plane wave approximation. In their models, Q_S decreases with depth to minimum values of 80 ± 15 in the 50–110 km depth range below 0–4 Myr old lithosphere (Figure 1). They attribute their higher intrinsic Q_S values than found in other studies to underestimated scattering effects in global-scale models.

[10] Below we first discuss our modeling methods and sensitivity of the predicted isotropic seismic structure to seismic attenuation and the presence of melt. Next, we perform a qualitative comparison with seismic constraints on mantle structure below mid-ocean ridges. Anisotropy may contribute to laterally varying asthenospheric velocity anomalies [*Ekström and Dziewonski*, 1998], but we focus here on the first-order isotropic structures. Imaged seismic structure is strongly influenced by the distribution and type of data, and the parameterization and regularization in the inversion. Therefore, we also test how our synthetic seismic ridge structures would be resolved if subjected to the type of inversions applied to the MELT/GLIMPSE data. *Harmon et al.* [2009] used the Rayleigh wave data from this experiment to invert for a representative 2-D cross section as a function of age from the ridge (Figure 1). Given the two dimensionality and symmetry of our dynamic models, this is the most appropriate model to compare to.

3. Modeling Approach

3.1. Dynamic Spreading Model

[11] We model two-dimensional thermal and compositional mantle structure below a symmetrically spreading oceanic ridge, and include the effects of major element depletion and

melt fraction on density, and dehydration on rheology. We consider three cases with different mantle potential temperatures and water contents. Melt migration parameters are chosen to maximize retained melt fractions within geochemical and petrological constraints.

3.1.1. Model Setup

[12] We solve the equations for Stokes flow under the Boussinesq approximation in a 2-D Cartesian domain 1400 km long and 700 km deep for non-Newtonian solid mantle flow using an extended version of CitCom that tracks melt production and solid mantle composition as the system evolves [see *Armitage et al.*, 2008; *Moresi and Solomatov*, 1995; *Nielsen and Hopper*, 2004]. The model resolution is 257 by 257 constantly spaced nodes. Solid mantle flow boundary conditions are a free surface on the sides and base, and a prescribed divergent flow velocity condition on the top. Temperature boundary conditions are fixed temperature at the base (a mantle potential temperature of 1315 or 1415°C; Figure 2) and top (0°C), and a zero temperature gradient at the sides. The initial condition is of a 125 km thick lithosphere defined by a linear increase in melt depletion (from 0 to 50% representative of a continental buoyancy) and reduction in temperature from the basal temperature condition to 0°C at the surface. This initial lithosphere rifts and the model are run until an ocean basin of at least 1600 km width is formed. Solid mantle density is a function of temperature, melt fraction and melt depletion [see *Nielsen and Hopper*, 2004], providing buoyant flow due to melt generation. Likewise the non-Newtonian rheology is dependent on the melt fraction generated and the dehydration due to melt generation as defined by *Nielsen and Hopper* [2004].

[13] Melt production is calculated as a function of temperature, pressure and previous depletion [*Nielsen and Hopper*, 2004; *Phipps Morgan*, 2001; *Scott*, 1992]. Volatiles, such as water and carbon dioxide, lower the solidus causing the generation of deep melt and have been associated with the low seismic velocity zones imaged beneath both the oceans and continents [*Eggler*, 1976; *Lambert and Wyllie*,

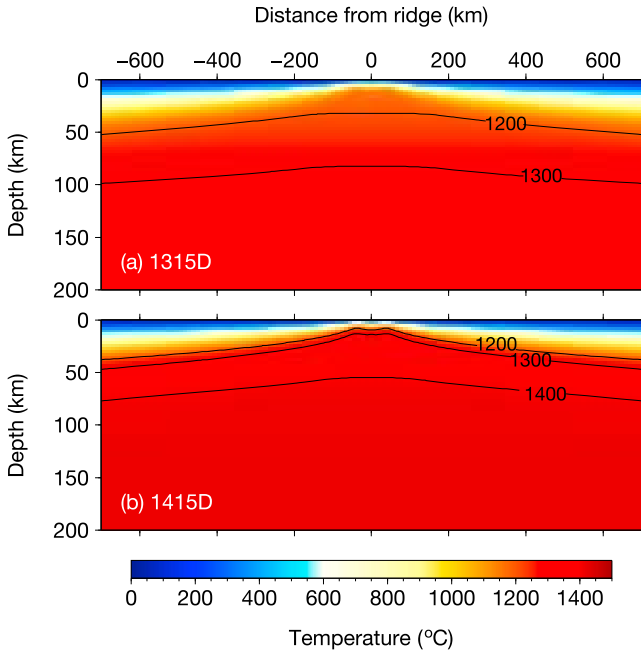


Figure 2. Modeled temperature for the two damp cases with potential temperature of (a) 1315°C (1315D), and (b) 1415°C (1415D). Temperatures from the wetter model (1315W) are almost indistinguishable from those of case 1315D.

1968; Wyllie and Huang, 1975]. Melt generation can be calculated using thermodynamic models such as MELTS and its derivatives [e.g., Asimow et al., 2004], or more simple parameterizations based on experimental data [e.g., Katz et al., 2003; McKenzie and Bickle, 1988; Scott, 1992]. These differing parameterizations produce somewhat different predictions of melt paths at low melt volumes and during hydrous melting. We are interesting in posing the general hypothesis that deep hydrated melting can cause reduced seismic velocities, therefore we use a more generalized parameterization that is designed to capture the most widely agreed characteristics of mantle melting, i.e., low-productivity melt generation for conditions below the dry solidus, and increasing productivity for increasingly hydrated mantle. The melt fractions generated (Figure 3) are comparable to those obtained with the more complete parameterizations [e.g., Asimow et al., 2004; Katz et al., 2003].

[14] We use the melting system as explained in Armitage et al. [2008, 2011] and Nielsen and Hopper [2004], where a wet and dry melting regime are defined and parameterized. We define two mantle hydrations: the first, *damp mantle*, model contains volatiles such that the solidus of volatile rich melting is 200°C cooler than the dry solidus and the dry solidus is reached at 2% melt depletion (Figures 3d and 3e, green lines). This corresponds roughly to a mantle with 1000–2500 H/10⁶ Si, or about 100–250 ppm H₂O by weight, where dehydration is thought to occur up until about 2% melt generation and the wet solidus is ~60 km below the dry solidus [Hirth and Kohlstedt, 1996]. Such an amount of water is typical of estimates for mantle water contents at spreading centers [Dixon et al., 1988; Michael, 1988, 1995; Robinson et al., 2001].

[15] The second, *wet mantle*, model has a volatile-rich solidus that is 350°C cooler than the dry solidus and the dry solidus is reached at 3% melt depletion (Figures 3d and 3e, blue lines). This roughly corresponds to a wet mantle (more than 3000 H/10⁶ Si or ~300 wt ppm H₂O), and depending on the importance of garnet on the water partitioning, such a change in the solidus temperature could correspond to a mantle with up to 1500 wt ppm H₂O [Hirschmann et al., 2009; Katz et al., 2003]. These two idealized systems are designed to emulate the complex interplay between water and melt productivity at mid ocean ridges, where increased water content increases bulk melt fractions generated but lowers productivity in the deep hydrous melting regime [Asimow et al., 2004; Hirschmann et al., 1999; Kelley et al., 2010].

[16] Following, for example, Spiegelman and McKenzie [1987], Scott and Stevenson [1989], Sparks and Parmentier [1991], and Jha et al. [1994] we assume melt flow, or compaction, can be adequately calculated by vertical Darcy flow. We use the implementation of Scott [1992], where melt fraction, ϕ , (by volume, also termed melt porosity) is subject to advection within the solid mantle and compaction due to vertical melt flow, v ,

$$\frac{\partial \phi}{\partial t} = -\mathbf{u} \cdot \nabla \phi - (1 - \phi) \nabla \cdot \mathbf{v} + \dot{m} \quad (1)$$

where \mathbf{u} and \mathbf{v} are vectors for the solid mantle creep, and the vertical flow of the melt, respectively and \dot{m} is the melt production rate. The vertical migration of melt is given by

$$\mathbf{v} = \frac{K_{\phi} \phi^n}{\mu} g (\rho_m - \rho_l) (1 - \phi) \hat{\mathbf{z}} \quad (2)$$

where g is the acceleration due to gravity, $\rho_m = 3340 \text{ kg/m}^3$ is the mantle density and $\rho_l = 2800 \text{ kg/m}^3$ is the melt density and $\hat{\mathbf{z}}$ is a unit vector in the vertical direction. K_{ϕ} is the coefficient that relates permeability to melt porosity and is a function of grain size, d ,

$$K = K_{\phi} \phi^n = \frac{d^2 \phi^n}{C} \quad (3)$$

[17] Estimates of grain size, the geometric constant C , and the exponent n vary. The exponent n is between 2 and 3 depending on the grain geometry [McKenzie, 1984]. Grain sizes within the mantle vary from the scale of centimeters to millimeters [e.g., Ahern and Turcotte, 1979; Behn et al., 2009]. Grain size has a large effect on melt retention, as for larger values the velocity of vertical migration is significantly increased. For $n = 2$ and for small grain sizes C has been numerically calculated to be ~3000 [Cheadle et al., 2004]. For $n = 3$, C is in the range 10 to 240 [Connolly et al., 2009; Wark and Watson, 1998]. Increasing the grain size will increase melt flow. Increasing n will reduce melt flow. But n is a function of pore space, which is controlled by the grain size, therefore it is difficult to upscale laboratory experiments to mantle processes. Recent experiments on very small fractions of melt generated within olivine-basalt aggregates of ~100 μm grain size suggest that the power law relationship is valid down to porosities of at least 0.02 [Zhu et al., 2011]. But grains within the mantle are likely up to 3 orders of magnitude larger [Behn et al., 2009] and the uncertainty of grain size causes estimates of melt velocity to

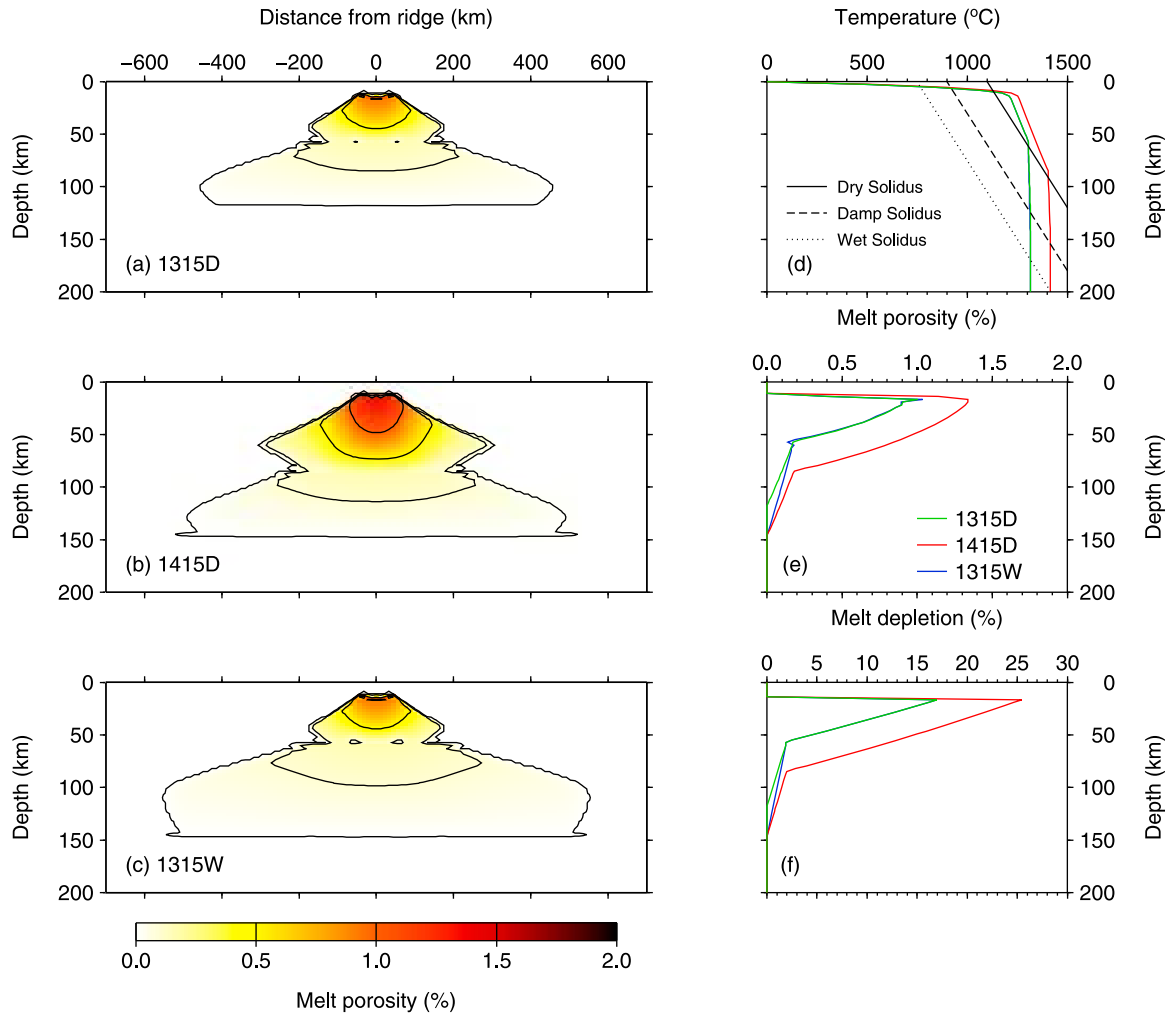


Figure 3. Retained melt and extent of depletion for the three cases: 1315D, 1315°C mantle potential temperature, damp; 1415D, potential temperature 1415°C, damp; and 1315W, 1315°C potential temperature, wet. (a–c) Geometry of the melt zone with contours of retained melt fractions (in percent). (d–f) Profiles below the ridge of temperature (Figure 3d), melt porosity (Figure 3e), and depletion (Figure 3f). Melt depletion contours are almost horizontal throughout the domain.

deviate by 2 orders of magnitude, from cm/yr to m/yr. Given the difference in scale between laboratory-scale experiments and mantle processes these parameters are poorly constrained. As we are interested in retaining melt to explore the cause of the low seismic velocities observed, we base our model on a lower estimate of grain size, $d = 1$ mm, which with $C = 3000$ gives $K_\varphi = 10^{-10}$ m² and $n = 2$ [Scott, 1992]. This provides upward velocities on the lower end (on the order of cm/yr) to allow for maximum melt retention, and are similar to those used in previous studies of the East Pacific Rise [Braun et al., 2000; Conder et al., 2002; Toomey et al., 2002].

3.1.2. Model Cases

[18] Most seismic data of subridge mantle structure available for comparison are from the East Pacific Rise and display substantial asymmetry in signatures west and east of the ridge axis [Dunn and Forsyth, 2003; Forsyth et al., 1998; Hammond and Toomey, 2003; Harmon et al., 2009]. However, in this paper we investigate how joint effects of a geodynamically plausible distribution of temperature,

hydration and melt affect seismic velocities by focusing on the simplest case of symmetric spreading at a half spreading rate of 72 mm/yr.

[19] We show the results for three distinct cases (Figures 2 and 3):

[20] 1. *1315D*: Damp model with potential temperature of 1315°C. This model is compatible with Pacific crustal thickness and commonly inferred MORB source hydration [e.g., Hirschmann, 2010; Hirth and Kohlstedt, 1996].

[21] 2. *1415D*: Damp model with a hot mantle, potential temperature of 1415°C, and same mantle hydration as case 1 (Figure 3, red line). This model would yield too high a crustal thickness but high mantle temperatures have been proposed as possible cause or contributing factor to asymmetry of the anomaly observed below the EPR [Conder et al., 2002; Toomey et al., 2002].

[22] 3. *1315W*: Wetter mantle of same potential temperature as case 1. The increased level of hydration changes the depth extent of melting by ~ 40 km but only changes total amount of melt produced and hence crustal thickness by

about 10% [e.g., *Asimow et al.*, 2004]. It may however have substantial velocity-lowering effects.

[23] Figures 2 and 3 display the thermal structure, retained melt fractions and extent of melt depletion for the three models. The thermal structures of models 1315D and W are almost indistinguishable, even though there are some differences in flow pattern as dehydration at different depths levels affects viscosity.

[24] In model 1315D, 1% melt depletion is reached at 85 km depth and dry melting starts at about 55 km depth coinciding with 2% melt depletion (Figures 3d and 3e, green lines). The maximum amount of melt depletion is about 20%, resulting in a harzburgitic composition of the residue, and if all melt were extracted, sufficient melt to generate an 10 km thick crust. To generate a 6 km thick crust would require lowering potential temperature to 1275°C, which is lower than the most recent petrological estimates of the temperature of a MORB source mantle [*Herzberg et al.*, 2007]. This indicates that melt extraction is likely incomplete and some remains frozen in the lithosphere.

[25] With our parameterization of melt migration, up to 0.08% melt is retained in the wet-melting region of model 1315D, and significant melt fractions exceeding 0.1% are only retained in the depth range of dry melting (Figure 3a). These numbers are compatible with the low wet-melting productivity estimates from petrological constraints [*Asimow et al.*, 2004; *Hirschmann*, 2010]. To retain much larger melt fractions would require either that the grains are more poorly interconnected than high-pressure experiments would indicate [*Wark and Watson*, 1998; *Zhu et al.*, 2011] or that grain sizes are smaller than 1 mm. Given that if anything, grains are likely to be larger than 1 mm [*Behn et al.*, 2009] and Ra, Pa and Th isotopes suggest efficient melt extraction [*Connolly et al.*, 2009; *Faul*, 2001], it is hard to argue that melt porosities within the deep mantle below 50 km depth can be much higher than we calculate.

[26] In the hotter model, 1415D, melt depletion reaches 1% at a depth of 110 km, and dry melting starts at a larger depth, 80 km (Figures 3d and 3e, red lines). Although the region over which melt is retained increases in size (Figure 3b), damp melting remains low in productivity and the maximum fraction of retained melt is not higher than in case 1315D.

[27] In the wetter model, 1315W, the extent of the wet melting region is larger again than either of the two other models. 1% melt depletion is already reached at a depth of 125 km. However, dry melting starts at a similar depth as in case 1315D (Figures 3d and 3e, red lines). Maximum retained melt fractions in the wet-melting region now reach up to 0.2–0.3% (Figure 3c).

3.2. Conversion to Seismic Velocity

[28] To compute mantle seismic velocities for the model, we consider anharmonic and anelastic effects of temperature, pressure, major element composition, hydration and phase. We consider only isotropic velocities, because constraints on anisotropic elastic constants and anisotropic attenuation are much more limited. We will only discuss the shear velocity and attenuation structures, although the method also yields V_P and density. To get full temperatures from the dynamic models, we add an adiabatic temperature gradient of 0.45 K/km to the Boussinesq potential temperatures,

which gives a good approximation for the effect of adiabatic compression down to about 400 km depth.

3.2.1. Anharmonic and Melt Effects

[29] Phase diagrams and anharmonic velocities are calculated using the code PerPleX [*Connolly*, 2005] and the equation of state, solid solution models and 2008-NaCFMAS mineral parameter database from *Stixrude, Lithgow-Bertelloni and coworkers* [*Stixrude and Lithgow-Bertelloni*, 2005; *Xu et al.*, 2008]. Major element composition is parameterized as a function of the degree of melt depletion. The composition is assumed to be pyrolytic for less than 1% melt depletion, and changes via a pyrolyte-harzburgite mechanical mixture to a pure harzburgite by 20% melt depletion (compositions from *Xu et al.* [2008]). Differences in seismic velocity for a pyrolytic and harzburgitic composition are small except where seismically very slow plagioclase is stable (shallower than ~30 km depth and almost absent in harzburgite). Hence the exact parameterization of the major element composition between an undepleted peridotite and a melt-depleted harzburgite has little effect on predicted seismic structure. Effects of water are only incorporated in anelasticity.

[30] To model the seismic effect of melt, we chose derivatives proposed by *Hammond and Humphreys* [2000b]. They found that relaxation in the presence of melt occurs by melt squirt and occurs on timescales that are less than seismic wave periods [*Hammond and Humphreys*, 2000a]. Experimental work indicates that other mechanisms, which do lead to an effect of melt on attenuation within the seismic frequency range, may actually be important [*Faul et al.*, 2004; *McCarthy and Takei*, 2011]. However, the observation of very low velocity and relatively low attenuation (i.e., high Q_S) below the EPR [*Yang et al.*, 2007] and possibly other ridges [*Dalton and Faul*, 2010] would be most compatible with an effect of melt on anharmonic velocities only.

[31] We chose from *Hammond and Humphreys* [2000b] the highest estimates for the sensitivity of V_S to melt applicable to melt fractions less than 1%, those for melt in organized cusped geometry: $-7.9\% \Delta V_S / \% \text{melt}$. At fractions exceeding 1%, a film-like melt geometry may lead to stronger drops in V_S , but only if the first melt fractions below 1% reside in tubules. For this case, velocity derivatives for fractions less than 1% are estimated to be only $-2.9\% \Delta V_S / \% \text{melt}$ [*Hammond and Humphreys*, 2000b]. Other studies have estimated shear velocity drops between -1 and -3% per percent of melt for what they considered to be plausible mantle melt geometries [*Kreutzmann et al.*, 2004; *Takei*, 2002]. By choosing the *Hammond and Humphreys*' [2000b] derivatives for a cusped geometry at all melt fractions we should thus get a high estimate of the effect of melt at asthenospheric depths, as at these depths, the melt fractions predicted from our models are below 1%. Consistent with these derivatives, we assume that melt does not affect seismic shear attenuation at seismic timescales; that is, we maximize the effect of melt on shear velocity and on minimize the effect of melt on attenuation.

3.2.2. Anelasticity

[32] At temperatures close to the mantle adiabat, anelasticity has a very strong effect on velocity, but it is more poorly constrained than the elastic properties [*Jackson and Faul*, 2010; *Jackson et al.*, 2002; *Karato*, 1993; *Karato and Spetzler*, 1990; *McCarthy et al.*, 2011]. We use three shear attenuation formulations, which we will denote as ' Q_F ', ' Q_g ' and ' Q_Y '.

[33] The first attenuation model, Q_F , is an experimentally carefully constrained formulation, taken from *Faul and Jackson* [2005] and *Jackson et al.* [2002]. We use it in the form and with the parameter values as proposed by *Behn et al.* [2009], who incorporated the effect of hydration, and adapted the grain size depth variation to reconcile it with observations on the depth extent of seismic anisotropy below oceanic lithosphere:

$$Q_F(\omega, T, P, C_{OH}, d) = \left[A_F \left(\frac{C_{OH}}{C_{OH}^{ref}} \right)^{r_Q} \left(\frac{d_{Q_{ref}}}{d} \right)^{p_Q} \omega^{-1} \cdot \exp \left(- \frac{E_Q + pV_Q}{RT} \right) \right]^{-\alpha_F} \quad (4a)$$

$$A_F = B_0 d_{Q_{ref}}^{-p_{Q_{ref}}} \exp \left[\frac{(E_Q + p_{Q_{ref}} V_Q) - (E_{Q_{ref}} + p_{Q_{ref}} V_{Q_{ref}})}{RT_{ref}} \right]. \quad (4b)$$

[34] This Q_S model depends on (depth-dependent) grain size d , hydration C_{OH} , wave frequency ω and on temperature T and pressure P via an exponential Arrhenius factor. R is the universal gas constant, and all the other parameters: prefactor B , exponentials r_Q , p_Q and α_F , and activation energy E_Q and volume V_Q , are constrained through fits to experimental data [*Behn et al.*, 2009]. For dry mantle, we take $C_{OH} = 50$ H/10⁶Si, for damp mantle we choose $C_{OH} = 1000$ H/10⁶Si, and for wet mantle $C_{OH} = 3000$ H/10⁶Si compatible with concentrations used in other studies [*Behn et al.*, 2009; *Hirschmann*, 2010]. We use a linearized grain size versus depth relation, where d increases from 1 cm at 100 km to 2.5 cm at 400 km. These are based on the profiles modeled by *Behn et al.* [2009], without the increase in grain size in the cooler lithosphere, which is thin in our near-ridge models.

[35] This unfortunately creates a minor disconnect between the dynamic model (where d constant and equal to 1 mm) and the attenuation model ($d \sim 1$ cm). There are two reasons for not adding this final piece of self-consistency into the models: (1) There are many uncertainties in mantle grain size (see section 3.1) and the grain size dependence of both anelasticity and melt permeability. More recent experimental anelasticity models [*Jackson and Faul*, 2010; *McCarthy and Takei*, 2011] differ in grain size sensitivity from model Q_F as used here. Given these uncertainties we do not feel it is warranted to attempt to adapt the formulations to make grain sizes consistent throughout the dynamic and seismic modeling. Note that reducing the grain size by an order of magnitude from cm to mm decreases Q by a factor of 1.8. The depth-dependent grain size in Q_F contributes to the depth sensitivity, and in this it trades off with the poorly constrained activation volume. (2) Keeping the two melt and attenuation models independent allows for further comparison of attenuation models for the same base predictions of melt fraction, temperature, pressure and composition.

[36] The second attenuation model, Q_g , is a partly empirical model, which we include because it, and models very similar to it, have been quite successful in reconciling continental V_P , V_S , shear attenuation, and surface heat flow constraints [*Goes and van der Lee*, 2002; *Goes et al.*, 2000,

2005; *Hwang et al.*, 2009, 2011; *Shapiro and Ritzwoller*, 2004b; *van Wijk et al.*, 2008]:

$$Q_g(\omega, T, P, C_{OH}) = A_g \left(\frac{C_{OH}^{ref}}{C_{OH}} \right)^s \omega^{\alpha_g} \exp \left(\frac{\alpha_g \gamma T_m}{T} \right) \quad (5a)$$

where

$$\gamma T_m = E^* + PV^*. \quad (5b)$$

[37] This model depends on wave frequency, temperature and pressure. A homologous temperature (melting temperature T_m over T) formulation is used to prescribe the depth dependence of activation enthalpy in the Arrhenius factor [*Karato*, 1993] as an alternative to using activation volume V^* for which depth dependence is poorly constrained. The prefactor A_g has been set to yield Q_S values within the range of seismic 1-D models [*Cammarano et al.*, 2003] (similar to the procedure followed by *Matas and Bukowski* [2007]). The parameters for this model are $A_g = 0.1$, $\alpha_g = 0.15$, $\gamma = 38$. The values of Q_g are likely appropriate for a MORB source, i.e., somewhat damp mantle. To simulate the effects of dehydration we add to A_g a factor $(C_{OH}^{ref}/C_{OH})^s$, where $s = r_Q \alpha_F$ as in *Behn et al.* [2009], and we take as a reference value the C_{OH} for a damp mantle. This results in about a factor of three increase in Q_S from a damp to a dry mantle. For the solidus used to scale homologous temperature [*Herzberg et al.*, 2000], the Q_g model corresponds to a somewhat higher activation energy than the experiments from *Jackson et al.* [2002], however within the range of other experimental constraints [*Karato and Spetzler*, 1990].

[38] The third model we tested is the adaptation of the Faul and Jackson model that *Yang et al.* [2007] proposed to match their attenuation observations for the EPR. To achieve this they reduced the activation energy and the frequency dependence. We implement Q_Y as

$$Q_Y(\omega, T, P, C_{OH}, d) = Q_0 \left(\frac{C_{OH}^{ref}}{C_{OH}} \right)^s d^m \omega^{\alpha_Y} \exp \left(- \frac{\alpha_Y (E_Y + pV_Y)}{RT} \right) \quad (6)$$

where $Q_0 = 36$, $\alpha_Y = 0.1$, $s = r_Q \alpha_F$ as in the other two models, $d(z)$ follows the same linear profile assumed in our application of the Q_F model, $m = 0.27$, $E_Y = 250$ kJ/mole, $V_Y = 10$ mm³/mole. These parameters reproduce the curves as plotted by *Yang et al.* [2007] for the temperatures in our ridge model.

[39] The anelastic contribution is added to the velocity using the approximation for weakly frequency-dependent attenuation [*Minster and Anderson*, 1981]:

$$V(T, P, X, \omega) = V_{anh}(T, P, X) \left(1 - \frac{Q^{-1}(\omega, T, P, C_{OH}, d)}{2 \tan(\pi\alpha/2)} \right) \quad (7)$$

where V_{anh} is the anharmonic velocity from the thermodynamic approach (section 3.2.1) and Q is anelasticity from equations (4a), (4b), (5a), (5b), or (6) and α is the frequency exponent. This is a simplification from the full Kramers-Kronig relations [e.g., *Jackson and Faul*, 2010; *McCarthy et al.*, 2011].

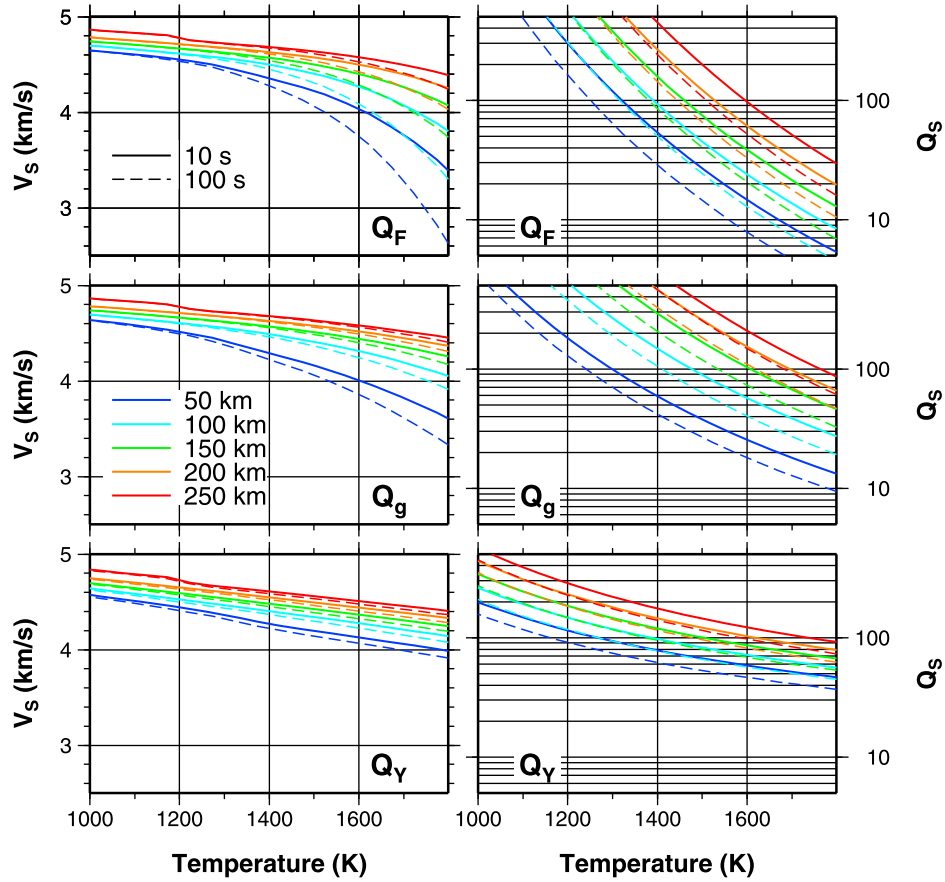


Figure 4. V_S and Q_S versus temperature for the three different attenuation models used, illustrated for two frequencies. In all cases, anharmonic velocities are for a pyrolitic mantle. The Q_F model is from *Behn et al.* [2009], based on the experimental work of *Jackson et al.* [2002] and *Faul and Jackson* [2005]. Curves displayed are for a water content of 1000 H/10⁶Si, appropriate for a MORB source mantle. The Q_g model is a more empirical model [*Goes et al.*, 2000; *van Wijk et al.*, 2008] that has yielded consistent thermal interpretations of a range of seismic models with heat flow. The Q_Y model is a modification of the model of *Faul and Jackson* [2005] proposed by *Yang et al.* [2007] to provide a match with the attenuation data for the EPR. The models differ in their strength of temperature, frequency and depth dependence.

[40] The behavior of the three Q_S models as a function of temperature and depth and their influence on V_S is illustrated in Figure 4, for two frequencies. At temperatures below 1500 K (the maximum used in the experiments of *Faul and Jackson* [2005]) the Q_F and Q_g models do not differ strongly. However, at higher temperatures and the lower frequencies the two parameterizations increasingly diverge. The stronger frequency dependence of Q_F , $\alpha = 0.27$ versus 0.15 for Q_g , leads to a stronger effective temperature dependence because activation enthalpy is scaled by the exponent of frequency. *Priestley and McKenzie* [2006] prefer an even stronger temperature dependence of attenuation at high temperatures, based on their comparison with experiments and a tuning of Q parameters for a thermal interpretation of their global V_S model. But they assume frequency independence in their formulation. Q_Y is lowest in temperature and frequency sensitivity and predicts the smallest ranges of V_S and Q_S . This model predicts only mildly temperature-dependent velocity-temperature derivatives, in contrast to models Q_F and Q_g .

[41] To obtain the same range of V_S values, model Q_F requires the largest range in intrinsic Q_S , while model Q_Y gives the smallest range. Interestingly, the V_S - Q_S trends *Dalton and Faul* [2010] obtained by comparing a global lithospheric attenuation and velocity model would be better matched by a frequency dependence like in model Q_g than in model Q_F . This is because in the theory used for the forward calculations V_S is proportional to Q_S^{-1} over the factor $\tan(\pi\alpha/2)$ (equation (7)); that is, the slope of these trends is largely determined by the frequency exponent α . Alternatively, a change in dominant anelastic deformation mechanism [e.g., *Jackson and Faul*, 2010] can lead to a change in Q - V_S slope as a function of temperature.

[42] In sum, model Q_F is most solidly grounded in experimental constraints, while empirical model Q_g is able to reconcile a wide range of observations, and model Q_Y is most consistent with EPR attenuation data. Anelasticity models from more recent experimental studies [*Jackson and Faul*, 2010; *McCarthy et al.*, 2011] fall within the range defined

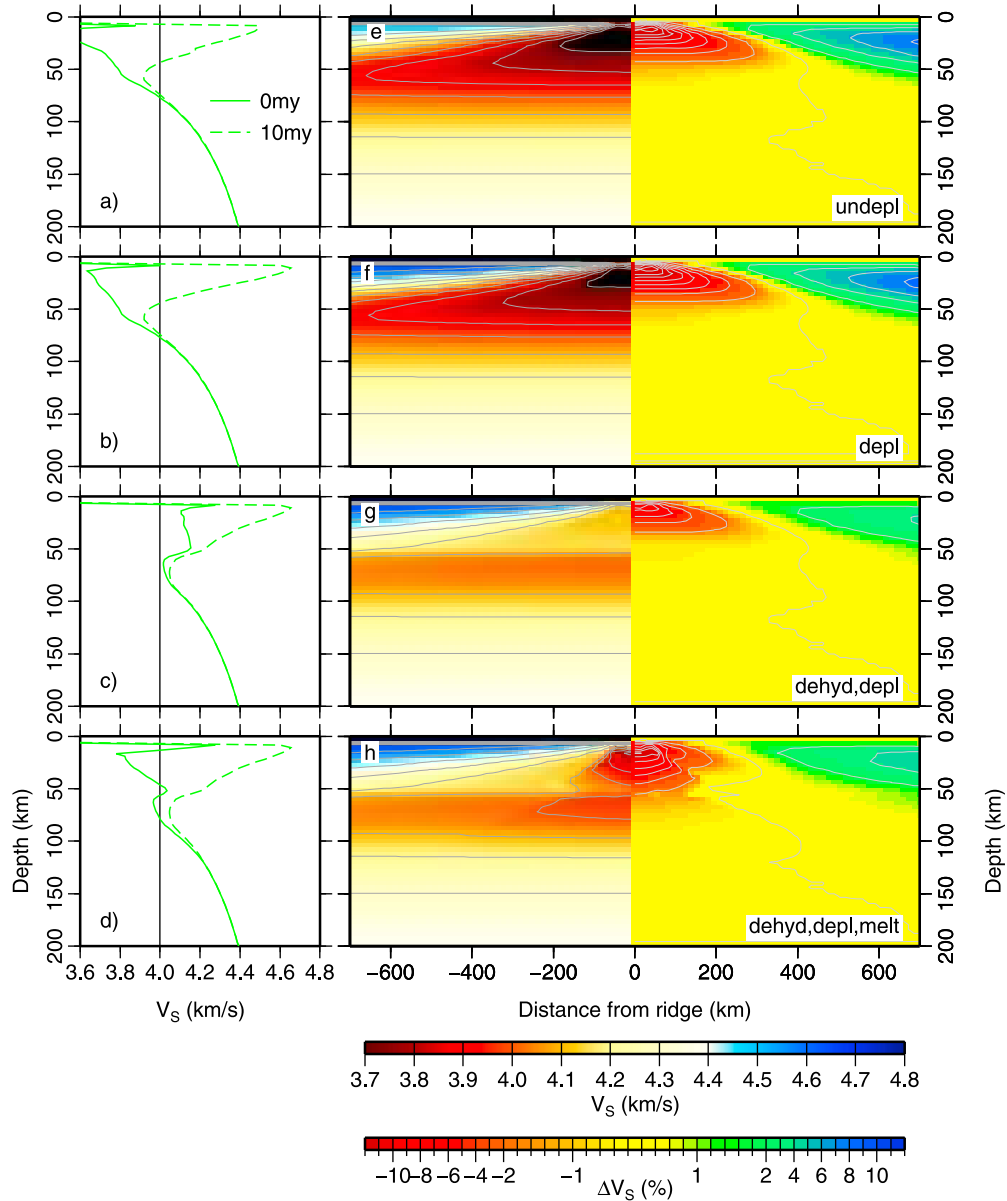


Figure 5. Seismic velocities calculated for the 1315D case using Q_g and a period of 50 s, illustrating the effect of adding major element melt depletion (compare Figures 5a and 5e with Figures 5b and 5f), dehydration (compare Figures 5b and 5f with Figures 5c and 5g), and melt (compare Figures 5c and 5g with Figures 5d and 5h). (a–d) Profiles of absolute velocity at the ridge (cooling age 0 Myr) and 700 km distance from the ridge (cooling age ~ 10 Myr). (e–h) (left) Absolute shear velocity, with contours every 0.1 km/s and (right) shear velocity anomaly relative to the regional model average (between ± 700 km from the ridge), with contours every 2%. Both major element and water depletion above 85 km depth increase velocities at shallow depth and reduce the anomalies. The presence of melt has only minor effects on the low-velocity zone below 50 km depth, but adds a pronounced shallow low-velocity anomaly.

by these three Q models in terms of their temperature, pressure, and frequency sensitivity. We will use the three to provide an illustration of how the uncertainty in attenuation models affects velocity structure.

3.3. Resolution Testing

[43] A qualitative comparison between synthetic and imaged seismic structure gives first insights into whether models and observations may be compatible. However, resolution of the imaged structures is affected by nonuniform

data distribution, the sensitivity of the waves used, as well as the regularization and parameterization applied in the inversions. The strongest constraints on mantle structure below spreading ridges come from surface wave analyses, and the best resolution achieved to date has been from regional experiments like those on the southern East Pacific Rise. To assess the effect of resolution limitations, we process the synthetic models using similar procedures as used in the EPR seismic studies to demonstrate the effects of the inversion

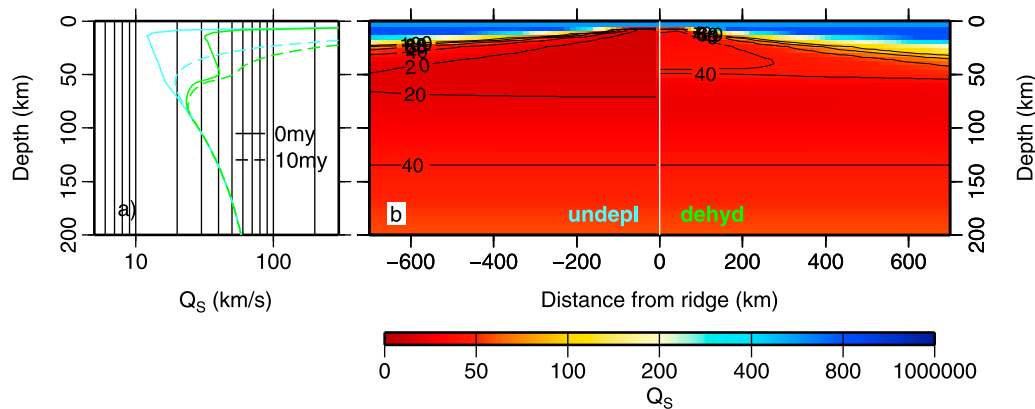


Figure 6. Seismic attenuation calculated for the 1315D case using Q_g and a period of 50 s, illustrating the effect of dehydration. (a) Profiles of Q_s at the ridge (cooling age 0 Myr) and 700 km distance from the ridge (cooling age ~ 10 Myr) for the case without water depletion (in cyan: as used for the velocity structure in Figures 5a, 5b, 5e, and 5f), and the case where dehydration by melting is accounted for (in green: as used in Figures 5c, 5d, 5g, and 5h). (b) The attenuation structure for the (left) undepleted case and (right) dehydrated case. Water depletion above 85 km depth increases Q_s at shallow depth and generates a high-attenuation (low Q_s) channel instead of a wedge.

and the broad depth sensitivity of Rayleigh waves on imaging structure.

[44] To generate a shear velocity model at a comparable resolution to *Harmon et al.* [2009], we calculate the predicted phase velocities directly from the synthetic velocity and density models, and then invert for shear velocity structure. At each period, τ (16–100 s), we calculate the phase velocity for the frequency-dependent synthetic V_p , V_s , and density at each distance from the ridge in 1-D using DISPER80 [Saito, 1988]. We choose this method rather than calculating full synthetics from a 3-D model, and then performing the tomographic inversion for phase velocity. This choice is motivated by the well-resolved phase velocity tomography in *Harmon et al.* [2009], owing to good event azimuthal coverage and small numbers of parameters, suggesting we would recover the input structure if we did perform full synthetic tomography.

[45] We construct the synthetic 2-D shear velocity profiles across the ridge by combining 1-D shear velocity inversions at each distance from the ridge. We invert the synthetic phase velocities for shear velocity at each distance from the ridge using the same model parameterization (layer thickness), and minimum curvature damping in the iterative damped least squares inversion with an a priori damping of 0.2 km/s. We calculate the partial derivatives of phase velocity with respect to shear velocity in depth using DISPER80 [Saito, 1988], using the starting model from *Harmon et al.* [2009]. The inversion is run for three iterations, which is sufficient for the models to converge. This procedure provides an illustration of the horizontal and vertical tomographic resolution that would be achieved if our model structures were probed with a data set similar to that collected at the EPR.

4. Synthetic Velocity and Attenuation Structure

[46] We first present how the seismic structure of subridge mantle is affected by the physical characteristics, temperature, composition and melt of the ridge models and do a qualitative comparison with subridge shear wave velocities

and attenuation. In section 5 we discuss tomographic resolution effects.

4.1. Effects of Melt Depletion and Melt Retention

[47] Figure 5 illustrates how the depletion of basaltic components and water by melting, and the retention of melt affect seismic velocity structure. We show results for attenuation model Q_g , which has an effect on predicted shear wave velocities that is in between the end-member frequency and temperature dependence of Q_F and Q_Y (Figure 4). Figure 6 shows the accompanying anelasticity structure, while Figure 7 shows results for the hotter and wetter models. A comparison between velocity and attenuation profiles for the three attenuation models is shown in Figure 8 and discussed in section 4.2.

[48] Without any major element or water depletion (Figures 5a and 5e), thermal effects lead to a large triangular low-velocity zone, with two minima. The shallowest V_s minimum corresponds to a depth range where plagioclase is stable. The deeper minimum is a classical low-velocity zone governed by a maximum in solid state attenuation (minimum Q_s) due to high temperature at relatively low pressure (Figure 5a). Velocity anomalies relative to the regional model average (Figure 5e, right) are mainly confined to depths less than 50 km.

[49] The depletion of basaltic components (Figures 5b and 5f) removes the shallowest minimum in V_s , because there is little plagioclase stable in a harzburgitic composition. However, the anomalies in velocity (Figure 5f, right) are barely different from the undepleted case because the average velocities used as regional reference change as well.

[50] Adding the effects of dehydration on Q (Figures 5c and 5g) substantially increases velocities above 52 km depth, introducing a velocity step. This shifts the minimum in Q_s downward below the ridge (Figure 6), leaving a low-velocity and low- Q_s zone that is quite constant in depth extent and varies only mildly in amplitude across the model. The sharpness of the step is controlled by the depth range over which dehydration occurs (i.e., how efficiently water partitions into

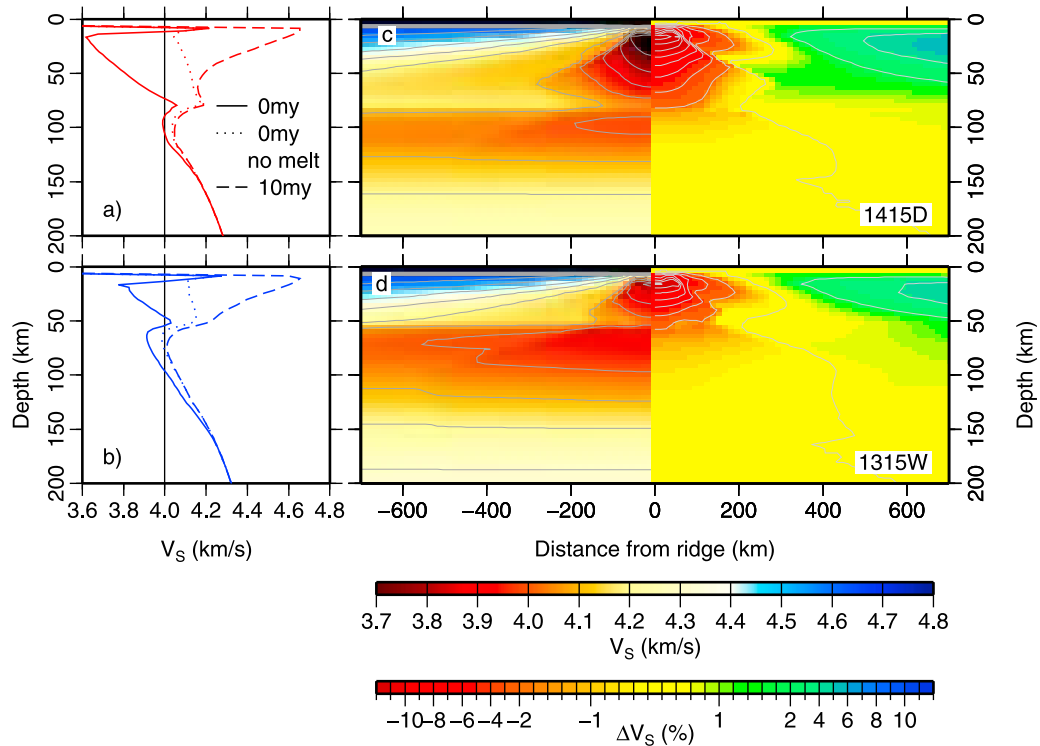


Figure 7. Absolute shear velocity and shear velocity anomalies for (a and c) models 1415D and (b and d) 1315W including effects of major element depletion, dehydration and melt using attenuation Q_g . Profiles and contours as in Figure 5. Figures 7a and 7b additionally include subridge profiles without the effect of melt (dotted). Compared with case 1315D (Figures 5d and 5h), the hotter model results in substantially lower velocities and a stronger, slightly deeper melt-associated anomaly. In the wetter model 1315W, the deep low-velocity zone is broadened, but the melt-induced anomaly is not substantially larger than in the dryer case (but note that the regional reference model is slower than for case 1315D).

the melt). The velocity step rapidly decreases with increasing lithospheric age, as the effect of anelasticity on V_S diminishes with decreasing temperature (compare 0 and 10 Myr profiles in Figures 5c and 6a). The shallow low-velocity anomaly (Figure 5g, right) is strongly reduced in amplitude compared to the hydrous case.

[51] Finally, adding the effect of retained melt on seismic velocity (Figures 5d and 5h) results in a strong low-velocity region in the region of dry melting, and mildly lowers the velocities in the deeper low-velocity zone right below the ridge (Figures 5d and 5h). When plotted as anomalies to the regional average, the dry-melting zone leaves a strong seismic anomaly with a complex shape, because the melting zone and the zone where temperatures are high relative to the regional average do not exactly coincide. The deeper melt region only increases seismic anomalies by a few tenths of a percent, in spite of the assumed strong melt retention and strong seismic sensitivity to melting.

[52] In the hotter model 1415D (Figures 7a and 7c), overall mantle seismic velocities are lower than in case 1315D (Figures 5d and 5h), and the dry-melting low velocity and the high-attenuation (low Q_S) deeper low-velocity zone are both more pronounced (Figure 7a). However, seismic anomalies relative to the regional average still mainly reflect the dry-melting zone, although this does extend to a larger depth than in case 1315D (Figures 7a and 7c).

[53] In the wetter model 1315W (Figures 7b and 7d), the high-attenuation, low-velocity zone is larger in depth extent than the other two models (Figure 7d). In addition, the higher melt productivity and resulting higher fractions of retained melt in the wet-melting region lead to an anomaly up to 1% in the wet melt zone (Figures 7b and 7d).

4.2. Role of Attenuation

[54] Figure 8 compares velocity and attenuation profiles for the three different attenuation models applied to the three ridge model cases 1315D, 1415D and 1315W, with each other and with the seismic constraints from global and EPR analyses. The three Q_S formulations all predict a double low-velocity zone, one below the dehydration boundary and one above [see also *Yang et al.*, 2007]. However, the relative amplitude of the two zones varies strongly with the Q_S model used.

[55] Below the ridge, model Q_F predicts the shallowest, melt-dominated, low-velocity zone to be similar in amplitude to the asthenospheric, attenuation-dominated, low-velocity zone. Models Q_g and Q_Y predict a less pronounced low-velocity zone in the asthenosphere. These differences are the result of the differences in the temperature and pressure sensitivity of the three formulations (Figure 4). In general, lower velocities are associated with lower Q_S values, however frequency dependence does have an additional effect (equation (7)).

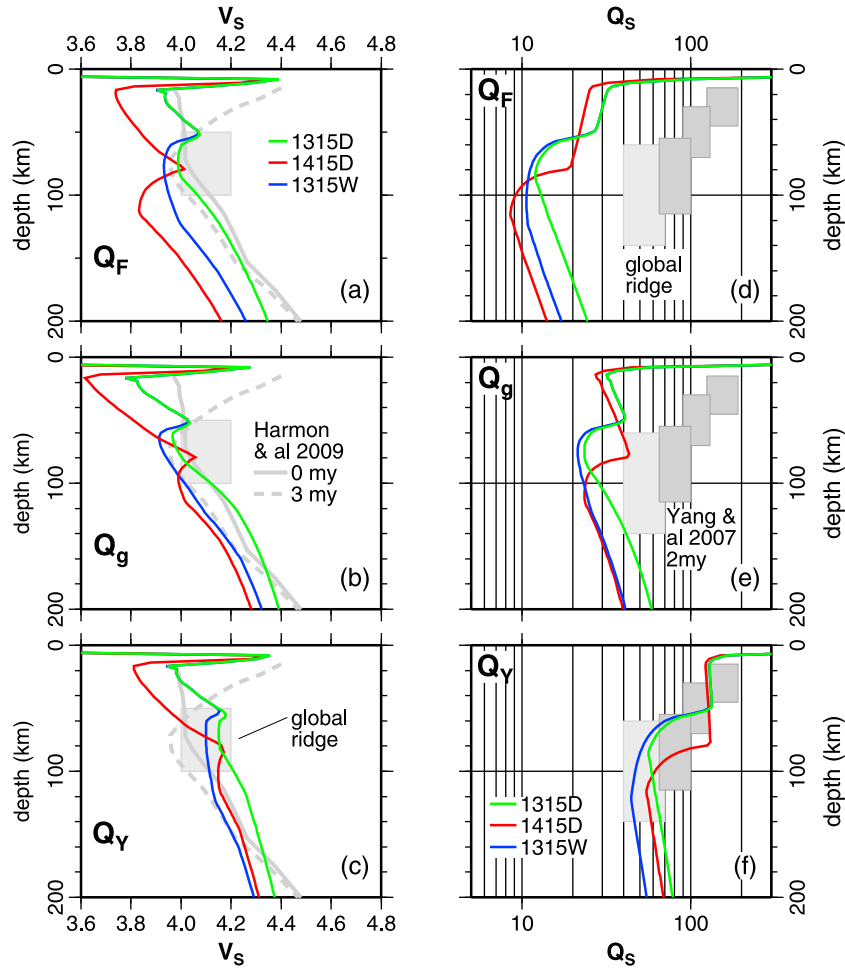


Figure 8. Comparison of (a–c) synthetic absolute shear velocities and (d–f) shear attenuation along profiles below the ridge calculated using the three different Q_S models, for a period of 50 s. Figures 8a and 8d, Figures 8b and 8e, and Figures 8c and 8f show anelasticity models Q_F , Q_g and Q_Y , respectively. Curves are for spreading models 1315D (green), 1415D (red) and 1315W (blue). All model lines include the effect of major element depletion, dehydration and melt. For all Q models, melt and dehydration result in a double attenuation maximum and velocity minimum. For comparison, imaged subridge velocity profiles (Figures 8a–8c) and Q_S (Figures 8d–8f) below the EPR are shown in dark gray, and the range of minimum V_S and Q_S from global studies in light gray. EPR V_S profiles are from the model of *Harmon et al.* [2009], directly below and just west of the ridge (Figure 1), Q_S estimates are for 0–4 Myr old lithosphere from *Yang et al.* [2007]. Synthetic profiles for Q_F and Q_g resemble imaged velocities, but do not match imaged Q_S , while profiles for Q_Y match imaged Q_S but do not reproduce the imaged low-velocity zone.

[56] The higher water content of model 1315W lowers Q_S and thereby V_S below the dehydration boundary compared to model 1315D (Figure 8). The higher temperatures in model 1415D also lower Q_S and V_S relative to model 1315D, and increased melt production additionally lowers V_S . However, around 80 km depth, the deeper dehydration in model 1415D results in a higher Q_S and higher velocity than in the cooler 1315D model.

[57] All Q models were tailored to have a similar sensitivity to water content of about a threefold decrease in Q going from damp to wet. Model Q_F predicts a stronger signature of a 100° potential temperature increase than the signature of a factor 3 higher water content (Figure 8). By contrast, with model Q_g the higher temperature and higher water content have effects of similar magnitude on attenuation and shear velocity, except that the depth of dehydration

is different in the hot (1415D) than wet (1315W) case. Model Q_Y is less sensitive to temperature than water content.

[58] Minimum asthenospheric velocity values with model Q_F are between 3.8 and 4.0 km/s, with model Q_g between 3.9 and 4.0 km/s and with Q_Y between 4.1 and 4.2 km/s. The ranges from Q_F and Q_g coincide with observed subridge minimum mantle velocities from global and regional models (section 2 and Figure 8), while the range from Q_Y is at the upper end of the global estimates. However, this comparison does not yet take into account any imaging effects that may bias observed minimum velocity values.

[59] Minimum asthenospheric Q_S values for the reference case 1315D are as low as 10–15 for Q_F , 20–30 for Q_g and 50–60 for Q_Y . The asthenospheric anelasticity values from models Q_F and Q_g are lower than the global large-scale estimates, although the substantial damping in global models

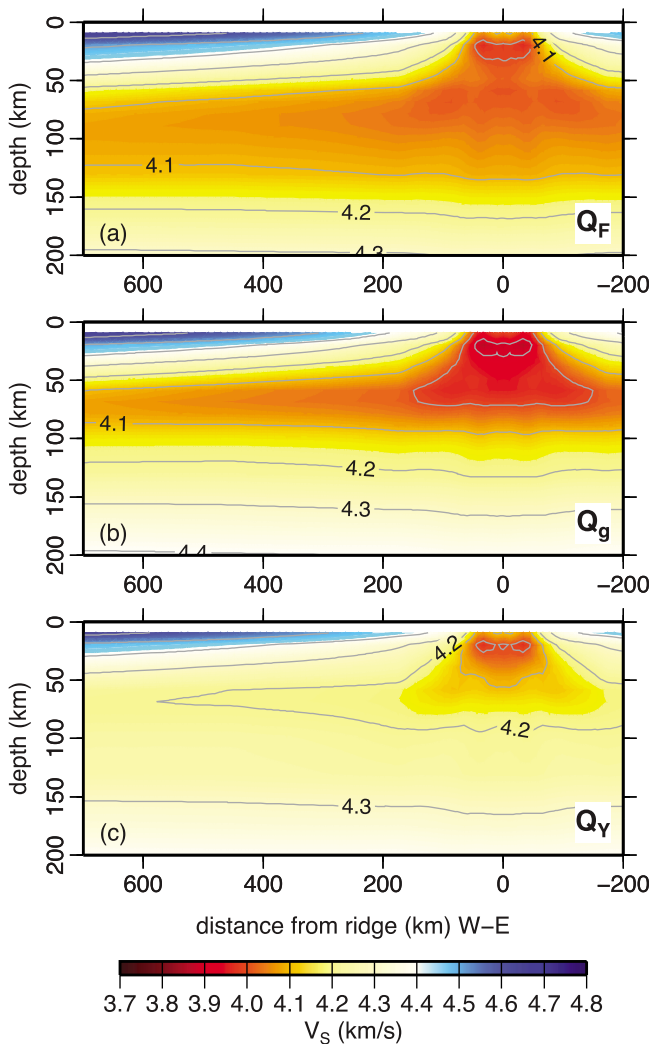


Figure 9. Synthetic tomographic image for model 1315D for the three attenuation formulations (a) Q_F , (b) Q_g , and (c) Q_Y . Compare with imaged velocity in Figure 1, bearing in mind that our model structures are symmetric.

probably means that these underestimate attenuation (i.e., overestimate Q). The Q values of Q_F and Q_g are however also much lower than those from the regional ridge attenuation model by *Yang et al.* [2007]. The Q_Y model, which was tailored to the regional ridge attenuation constraints, is most compatible with the range of global and regional Q_S constraints.

5. Synthetic Resolution of Shear Velocity Structure

[60] Examples of how our synthetic structures would be imaged with the inversion of *Harmon et al.* [2009] are shown for model 1315D and the three different anelasticity models in Figure 9. These can be compared in amplitude and depth range of the low velocities in the actual image (Figure 1), with the caveat that the synthetic model is symmetric. A quantitative comparison is easier for profiles through the synthetic tomography and actual imaged structure (Figures 10 and 11).

[61] In general, the synthetic structure is recovered well in terms of both amplitude and size of the velocity features. For all three Q models, the shallow, melt-related, low velocities are partially recovered, most strongly for model Q_g , which also has the strongest original dry-melting low-velocity zone. Most striking of the synthetic tomograms in Figure 9 is how different they are in the strength and depth extent of the deeper low-velocity channel. The low-velocity zone recovered from model Q_F is largest in depth extent, while the already much less pronounced deeper low-velocity channel in model Q_Y is barely recovered in the synthetic tomography.

[62] Most imaged velocity structures below young ocean floor/ridges comprise a single minimum in velocity at asthenospheric depths [Dalton et al., 2009; Gaherty and Dunn, 2007; Gu et al., 2005; Harmon et al., 2009; Maggi et al., 2006; Nishimura and Forsyth, 1989; Ritzwoller et al., 2004; Wang et al., 2009]. The resolution tests done for the MELT/GLIMPSE Rayleigh wave inversion illustrate how sensitivity of the waves and regularization could smooth out the double

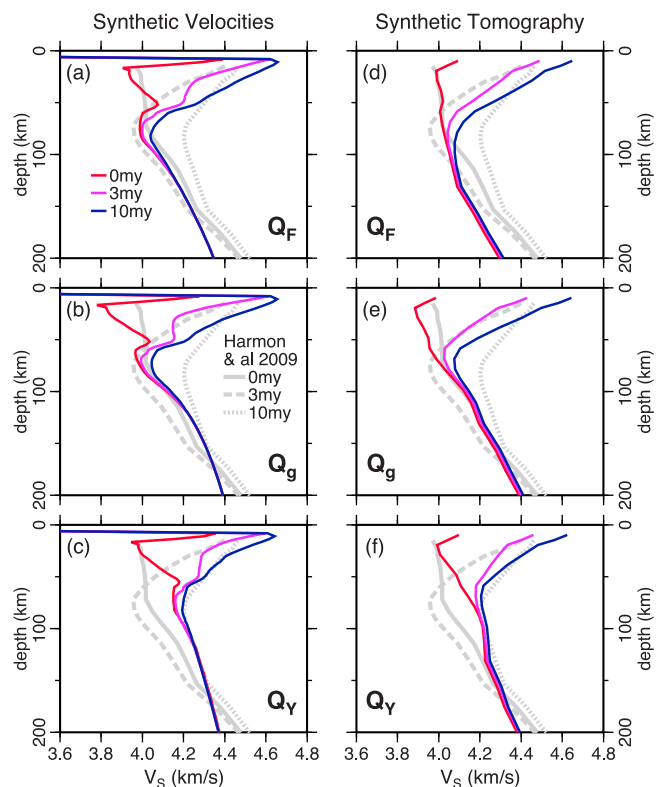


Figure 10. (a–c) Comparison of synthetic velocity profiles for model 1315D and (d–f) the same profiles recovered in a tomographic resolution test, in color, with the imaged profiles west of the ridge from *Harmon et al.* [2009], in gray. Figures 10a and 10d are for attenuation model Q_F , Figures 10b and 10e are for attenuation model Q_g , Figures 10c and 10f are for model Q_Y . Synthetic profiles shown are for a period of 50 s, but the resolution test takes into account variations of velocity as a function of frequency. Upon input, synthetic models 1315D- Q_F resemble the images most closely, however after accounting for resolution, models 1315D- Q_g provide a better match, due to their stronger increase of velocity with depth.

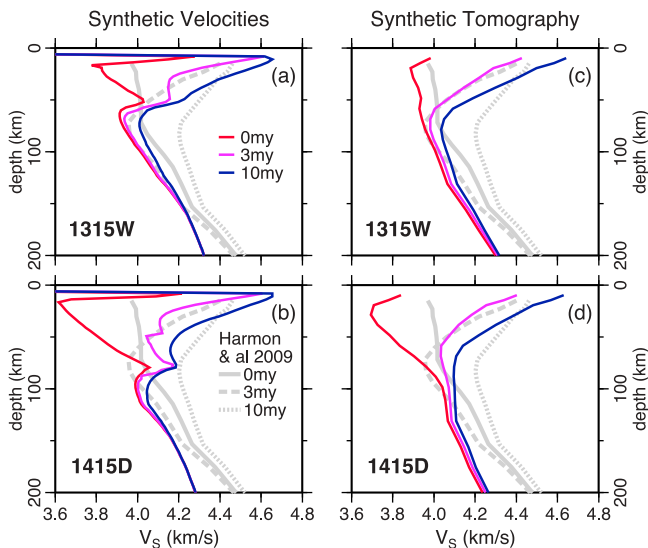


Figure 11. (a and b) Comparison of synthetic velocity profiles for model 1315W- Q_g and 1415D- Q_g and (c and d) the same profiles recovered after a tomographic resolution test, in color, with the imaged profiles from *Harmon et al.* [2009], in gray. Input synthetic profiles shown are for a period of 50 s, but the resolution test takes into account variations of velocity as a function of frequency. Although the damp models with a potential temperature of 1315°C resemble velocity structure below the ridge reasonably well (Figure 10), some variability in mantle water content and temperature might help account for imaged lateral variations in asthenospheric V_S .

anomaly into a single one that predominantly reflects the deeper asthenospheric minimum (Figure 9). Rayleigh wave dispersion data over a similar frequency range (but with considerably less dense coverage) underlie most of the ocean-scale models that imaged subridge structure, as well as the regional images below the Gulf of California. With the dense EPR data set, some of the shallow velocity minimum is imaged, as shown better by *Yang et al.* [2007]. The regional Love wave data set used by *Dunn and Forsyth* [2003] has a much stronger sensitivity to the shallow structure and resolves a very strong shallow low-velocity zone. For sparser data sets, the shallow melt-dominated anomaly would be mostly invisible.

[63] Another effect illustrated by the resolution tests is that of frequency-dependent depth sensitivity; that is, the effect that the deeper structure is mainly constrained from the longer period data. If Q_S is as frequency dependent as in model Q_g and especially Q_F , that means a deep structure is sampled by relatively slow low-frequency waves, while shallower structure is mapped by relatively fast higher-frequency waves. This results in a lower recovered velocity-depth gradient than that present in the actual synthetic velocity structure at constant frequency (Figures 10 and 11). For model 1315D, attenuation model Q_F predicts velocity-depth profiles more similar to the actual imaged profiles, however, Q_g provides a better match to the depth extent of the low-velocity zone after seismic resolution is accounted for. Recent seismic analyses indicate that frequency dependence in the 10–100 s period range has an exponent α between 0.2 and 0.3 [*Lekić et al.*, 2009; *Zaroli et al.*, 2010]; that is, this effect is likely important. Thus the synthetic tomography

clearly shows that seismic data require Q_S to increase more strongly with depth than in models Q_F and Q_Y .

[64] In terms of average amplitude and depth extent, model 1315- Q_g has most similarity with the imaged structure. However, in the upper 30 km, all three Q models match the spread of imaged mantle velocities below ocean floor ranging from 0 to 10 Myr old (Figures 10d–10f), while below about 60 km all of the models predict a smaller velocity range than imaged. The actual tomographic image (Figure 1) displays an increasing seismic velocity with age in the lithosphere, but shows no simple age trend in the asthenosphere. This complex structure has led to various interpretations in terms local lithospheric destabilization [*Harmon et al.*, 2011] or far-field asthenospheric flow [*Conder et al.*, 2002; *Toomey et al.*, 2002]. Our analyses reemphasize that there is significant 3-D structure in the mantle below and near the EPR superimposed on the structures predicted by a simple spreading model.

[65] Resolution effects on the hotter and wetter structures are similar. Models with a wetter mantle (Figure 11) may reproduce some of the lowest imaged velocities better, and a range of hydration from very wet to dry could match the imaged spread of velocities below 80 km depth. The 100° hotter models predict a larger range of velocities at 60–100 km depth than 1315D, but velocities that are much too low compared to the imaged EPR velocities at deeper depths. Several hundred degrees lower temperatures would be required to match the highest velocities at the western edge of the tomographic model.

6. Discussion

6.1. Reconciling Shear Velocity and Attenuation?

[66] No model is able to match EPR attenuation and velocity constraints simultaneously. This leaves two possible interpretations: (1) additional elastic velocity-weakening mechanisms play a role, as proposed by *Yang et al.* [2007] (2) the EPR results are not representative of subridge attenuation (although we cannot identify any aspects of the analysis by *Yang et al.* [2007] that justifies discounting their results).

[67] Which interpretation we choose does not just bear on our understanding of subridge structure, but on asthenospheric structure in general. Q formulations with a strong temperature dependence, like Q_F and Q_g , do not only match low asthenospheric velocities below ridges but also reproduce the range and depth distribution of seismic velocities with age under older oceans [*Behn et al.*, 2009; *Faul and Jackson*, 2005; *Priestley and McKenzie*, 2006; *Reynard et al.*, 2010; *Shapiro and Ritzwoller*, 2004b]. Furthermore, similar anelasticity formulations have also yielded reasonable temperature estimates below continents, where V_S , V_P models, surface heat flow data and xenolith thermobarometry can only be reconciled with the same thermal structure if Q_S is as temperature sensitive as models Q_F and Q_g [*Goes et al.*, 2000; *Priestley and McKenzie*, 2006; *Röhm et al.*, 2000; *Shapiro and Ritzwoller*, 2004a, 2004b].

[68] We illustrate this in Figure 12, where we show the velocities calculated for a simple lithospheric cooling model with a potential mantle temperature of 1315°C. The thermal parameters used are as in *McKenzie et al.* [2005] with plate thickness set to 400 km to simulate half-space cooling. Velocity calculations include the effect of dehydration, from

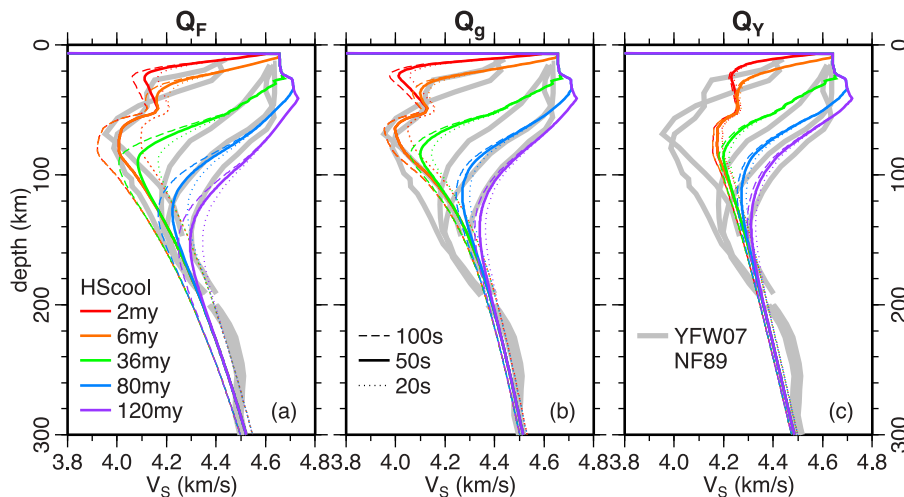


Figure 12. Synthetic 1-D shear velocity profiles (colored lines) calculated for a half-space cooling oceanic thermal model (thermal parameters from *McKenzie et al.* [2005]). Velocity calculations include the effect of dehydration progressing linearly from damp to dry between 85 and 52 km depth, and major element depletion by melt removal between 85 and 19 km depth. These are compared with imaged velocities from *Yang et al.* [2007] (above 190 km)/*Nishimura and Forsyth* [1989] (below 200 km) (gray lines). A temperature, pressure and frequency dependence like in experimental model Q_F or empirical model Q_g can reasonably reproduce the range of oceanic velocities with age above about 100–150 km depth without requiring melt. By contrast, a formulation like model Q_Y , which is consistent with EPR attenuation constraints, would require substantial additional elastic weakening mechanisms to explain low asthenospheric velocities over a wide range of ages.

damp to dry, progressing linearly between 85 and 52 km depth, and major element depletion by melt removal between 85 and 19 km depth, based on the depth ranges from model 1315D. The half-space cooling velocities are compared with the imaged velocities as a function of ocean-lithosphere age from *Nishimura and Forsyth* [1989] as plotted and supplemented with curves for 2 and 6 Myr by *Yang et al.* [2007], for a range of frequencies similar to that of the data used by these studies. Other seismic models yield similar velocity–ocean floor age distributions [*Maggi et al.*, 2006; *Ritzwoller et al.*, 2004]. Note that the *Nishimura and Forsyth* profiles were conditioned to be smooth and are thus not expected to contain kinks like we predict as an effect of dehydration, but the youngest profiles from *Yang et al.* [2007] did resolve such a kink.

[69] Of the three anelasticity models considered, anelasticity model Q_F , which was partially tailored to match oceanic velocity profiles [*Behn et al.*, 2009; *Faul and Jackson*, 2005], matches the imaged velocity range and depth trend best (Figure 12a). Note that the uncertainties in the synthetic velocity range with temperature and variation with depth are significantly smaller than uncertainties in absolute velocity values [*Cammarrano et al.*, 2003]. The data set used by *Nishimura and Forsyth* [1989] will likely lead to similar frequency-dependent resolution effects as that used by *Harmon et al.* [2009], where the resolved gradient is less strong than the actual gradient. Such resolution effects would deteriorate the match. The Q_g model (Figure 12b) does well at reproducing the velocity range at around 50 km depth, but overpredicts the imaged velocities below 100 km depth. In this case, tomographic resolution effects may improve the fit somewhat. Model Q_Y (Figure 12c) matches the velocities of the older ages (profiles of 36 Myr and older) well at depths around 50 km, but overpredicts velocities for the youngest

ages, where *Yang et al.* [2007] proposed a substantial melt contribution. As Q_g , Q_Y also predicts velocities that are too high below 100 km. In this case, our resolution tests showed that, because of the low-frequency sensitivity, imaging effects will probably not improve the match.

[70] As was already shown for the ridge model in Figure 8, model Q_F is substantially more attenuating than actually imaged Q values. Model Q_g is more attenuating above about 100 km depth but within the globally imaged range below this depth, while model Q_Y coincides best with the global and EPR attenuation estimates. While the Q_F and Q_g models misfit the EPR attenuation estimates, it is less clear that they are incompatible with other tomographic Q models, because of (1) the generally poorer resolution of attenuation than velocity models and (2) the difficulty of resolving the contributions of scattering and intrinsic attenuation to the variations of wave amplitudes. Regional studies often do resolve much stronger attenuation variations than global models, and the range found is quite consistent with Q_S variations predicted for thermal interpretations of imaged lithospheric and asthenospheric velocities with Q_g style attenuation [*Hwang et al.*, 2009, 2011]. However, although these attenuation images were correlated with tectonic and heat flow patterns, the data may contain a contribution from scattering if its effects are large scale and similarly correlated with tectonic features. Thus, if scattering contributes substantially to the attenuation patterns, then intrinsic attenuation would be too low to explain asthenospheric low velocities not just below ridges, but below older oceans and large parts of the continents as well.

[71] If attenuation cannot account for asthenospheric low velocities, other elastic velocity-weakening mechanisms

must play a role. For melt to contribute substantially to the low asthenospheric velocities, a factor of 3–5 higher melt retention would be required. This is problematic since in our models we already maximized melt retention and the sensitivity of shear wave velocities to melt. Furthermore, such high melt retention only helps to explain V_S and Q_S constraints if melt does not affect attenuation, something that is still debated [Faul et al., 2004; Hammond and Humphreys, 2000a; McCarthy and Takei, 2011]. If the velocity-lowering mechanism is the presence of melt, then the asthenosphere needs to contain pervasive melt fractions of at least 0.1–0.5%, assuming that seismic velocities have high melt sensitivities of $\sim 8\% \Delta V_S/\%$ melt. If seismic sensitivity were lower, higher melt fractions would be required. High seismic melt sensitivities are expected if melt is present in films along grain boundaries. However, at the same time, the high melt fractions implied require that migration of melt is much more inefficient than expected from our current understanding of melt transport, especially given that a film geometry tends to encourage melt migration. Hence, melt does not seem like a good candidate to explain asthenospheric velocities.

[72] Other mechanisms may play a role. For example, Reynard et al. [2010] showed that substantial elastic weakening is associated with a high-temperature phase transition in orthopyroxene. Although this mechanism likely only affects lithospheric and not asthenospheric velocities [Reynard et al., 2010], other mineral phase transitions may have similar effects in the asthenospheric P , T range.

[73] Crucially, the Q models that reproduce asthenospheric velocities without requiring large melt fractions or other elastic weakening parameters are the ones most closely constrained by experimental data. The only aspect of the experimentally constrained models that does not match the velocities well is the variation with depth. However, the experiments do not constrain pressure dependence. We tested increasing the activation volume of the formulations, but this does not improve the fit, as it also reduces temperature sensitivity above 150 km. So, a more nonlinear depth dependence appears required (note that the empirical parameterization of Q_g implies a V^* that changes with depth).

[74] Karato [2012] suggested that experimental attenuation models can actually generate a sharp velocity boundary akin to the seismically imaged ‘LAB’ discontinuity at the depth of dehydration, when assisted by a change in anelastic deformation mechanism from elastically accommodated grain boundary sliding (EBS) at low temperatures to diffusion creep at higher temperatures and depths. In tests with a version of model Q_F that includes the relaxation due to EBS [Jackson and Faul, 2010], we found that this mechanism did not enhance the jump. However, if we let dehydration in the oceanic cooling model occur over a narrow, few km, depth interval, at shallow depths (50–60 km) where attenuation effects are strongest, plus increase Q sensitivity to hydration ($r = 2$) this generates a sharper boundary than in the models we have presented. Although the jump gets increasingly smooth with age, it is possible to obtain a shear velocity step of several percent over a several km depth interval for oceanic lithosphere up to ages probably as large as 80–90 Myr.

[75] In summary, subridge and global asthenospheric velocity structure can be explained with very low amounts of retained melt, as preferred by petrological and geochemical

constraints, at temperatures that are consistent with those inferred from thermal models that fit heat flow and seafloor bathymetry, by a range of attenuation models that are consistent with experimental anelasticity data and with a range of seismic estimates of minimum asthenospheric Q_S . However, this interpretation does imply that the high Q_S inferred from the only detailed subridge attenuation study is somehow anomalous [Yang et al., 2007]. This analysis has not considered the effects of anisotropy (other than as an uncertainty on absolute isotropic velocity), which may vary with depth and age, may have implications for acceptable grain sizes [Behn et al., 2009] and may affect asthenospheric attenuation [Farla et al., 2012].

6.2. 3-D Structure

[76] Our models are for symmetric spreading above a homogenous mantle that only evolves in response to continued melt extraction. However, one of the most puzzling aspects of the MELT images has been their asymmetry, which the addition of GLIMPSE data has shown to be an expression of strong three dimensionality [Gu et al., 2005; Harmon et al., 2011]. From the magnetic anomalies seafloor spreading has been symmetric and the ridge is migrating westward at a rate of about 3 cm/yr [Scheirer et al., 1996]. Subsidence has been asymmetric with the western flank of the ridge subsiding more slowly than the eastern side. This is compatible with the imaged lithospheric structure, which appears slower and thinner on the western than on the eastern side, where the asthenospheric low-velocity channel is at a larger depth (Figure 1). The asymmetry has been attributed to motion of the deeper mantle, below the asthenosphere, relative to the ridge, resulting in a skewed passive mantle upwelling, enhanced by an influx of hot asthenosphere from the west [Carbotte et al., 2004; Conder et al., 2002; Toomey et al., 2002].

[77] In contrast to our spreading models, the lowest velocities imaged are offset from the ridge. Even in models where we imposed a migrating ridge, we found that the melt zone and with it the velocity minimum focused below the ridge, consistent with earlier modeling studies [Conder et al., 2002; Toomey et al., 2002]. Those earlier models focused on reproducing an asymmetric melt zone. However, as discussed above asthenospheric velocities may not carry a strong melt signature; that is, other factors likely cause the lateral variations in asthenospheric velocities and the asymmetry with respect to the position of the ridge. The hotter and wetter models show that the range of observed low velocities could be reproduced with some lateral variability in temperature or water content. Small lateral variations in physical conditions may also be sufficient to generate an asymmetric melt zone [Katz, 2010], which could explain the asymmetry of the low-velocity anomaly above 60 km depth imaged by [Dunn and Forsyth, 2003]. Variable temperatures or water content in the asthenosphere would be accompanied by lateral variability in retained melt content as well, but even in our wetter and hotter models, the retained amounts are $< 0.2\%$. Note that our choice of melt permeability parameters favored melt retention. For larger grain sizes (as inferred, e.g., by Behn et al. [2009]) melt migration would be more efficient and the asthenospheric low velocities would be even less

affected by the presence of melt. Furthermore, we chose relatively high values for the seismic sensitivity to melt.

7. Conclusions

[78] This study investigated whether imaged low velocities in the asthenosphere below mid-ocean ridges can be explained mainly with solid state attenuation and minor amounts of retained melt, as preferred by petrological and geochemical studies, or require significant amounts of retained melt suggested by several EPR seismic studies.

[79] For the three modeled scenarios of mantle structure below a spreading ridge comprising a damp MORB temperature mantle, a hotter and a wetter case, and three differing Q_S models there is a clear prediction of a double low seismic velocity zone (Figure 8). At shallow depths (between 20 and 40 km) the shear wave velocities drop to between 3.6 and 3.8 km/s at the ridge axis including a contribution from $\sim 1\%$ melt retention. At deeper depths, between 80 and 120 km, there is a second low-velocity zone with a V_S minimum of 3.8 to 4.1 km/s that has a magnitude that is little affected by the presence of $<0.1\%$ melt. Rather, the deeper velocity minimum is controlled by solid state attenuation in a hydrated mantle. High potential temperatures accentuate these low-velocity zones, as does the presence of greater amounts of deep melt in a hydrous case, yet this is a robust feature of all three modeled cases. Depending on the exact temperature and pressure dependence of the Q_S model and (regional) MORB source water content, the deeper (attenuation governed) minimum may even be the strongest one.

[80] Most seismic models under ridges (1-D, 2-D, and 3-D) found only a single low-velocity zone at depths between 50 and 150 km. Our resolution tests show that this is to be expected for Rayleigh waves with periods between 15 and 100 s, which form a core part of the data underlying many of the published oceanic-mantle models. Regional seismic models from the East Pacific Rise do find a double anomaly: a shallow one just below the ridge [e.g., Dunn and Forsyth, 2003], and a deeper one with a minimum at ~ 80 km depth [e.g., Harmon et al., 2009], but the signature is somewhat convoluted by the strong asymmetry of the sub EPR structure at the location of the MELT/GLIMPSE experiment from which these were derived.

[81] Synthetic velocity models that produce the range of observed low seismic velocities do require that attenuation in the deeper zone is also strong, with minimum Q_S values of 20–30. Such low Q_S values are inconsistent with Q_S estimates below the EPR by Yang et al. [2007], who after a careful correction for scattering required Q_S values of at least 65. However, they are not incompatible with the constraints from global models, backarc regional models and continental models (e.g., below the Basin and Range) [Dalton et al., 2008; Hwang et al., 2009, 2011; Sheehan and Solomon, 1992]. If the Yang et al. [2007] estimates of subridge intrinsic attenuation are correct, and other studies underestimate the contribution of scattering on attenuation, then the Q formulations that match their Q_S constraints extrapolated to conditions below older oceans or continents, would imply that the asthenospheric low-velocity zone elsewhere is also significantly affected by mechanisms other than solid state attenuation.

[82] However, if the Yang et al. [2007] Q_S estimates are non representative for subridge attenuation, then Q_S models that match experimental constraints on temperature, frequency and hydration dependence of attenuation can reconcile imaged asthenospheric seismic velocities and attenuation below ridges, older oceans and continents with damp thermal structures based on surface heat flow and seafloor bathymetry and geochemical and petrological constraints on melt productivity and mobility. Further work will be necessary to assess the contribution of anisotropy.

[83] **Acknowledgments.** We thank Don Forsyth, Bill Hammond, and an anonymous reviewer for their very thorough and constructive reviews. All figures were drawn using GMT [Wessel and Smith, 1998].

References

- Ahern, J. L., and D. L. Turcotte (1979), Magma migration beneath an ocean ridge, *Earth Planet. Sci. Lett.*, **45**, 115–122, doi:10.1016/0012-821X(79)90113-4.
- Armitage, J. J., T. J. Henstock, T. A. Minshall, and J. R. Hopper (2008), Modelling the composition of melts formed during continental break-up of the North Atlantic, *Earth Planet. Sci. Lett.*, **269**, 248–258, doi:10.1016/j.epsl.2008.02.024.
- Armitage, J. J., J. S. Collier, T. A. Minshall, and T. J. Henstock (2011), Thin oceanic crust and flood basalts: Reconciling observations from the northwest Indian Ocean, *Geochem. Geophys. Geosyst.*, **12**, Q0AB07, doi:10.1029/2010GC003316.
- Asimow, P. D., J. E. Dixon, and C. H. Langmuir (2004), A hydrous melting and fractionation model for mid-ocean ridge basalts: Application to the Mid-Atlantic Ridge near the Azores, *Geochem. Geophys. Geosyst.*, **5**, Q01E16, doi:10.1029/2003GC000568.
- Becker, T. W., B. Kustowski, and G. Ekström (2008), Radial seismic anisotropy as a constraint for upper mantle rheology, *Earth Planet. Sci. Lett.*, **267**, 213–227, doi:10.1016/j.epsl.2007.10.11038.
- Behn, M. D., G. Hirth, and J. R. Elsenbeck II (2009), Implications of grain size evolution on the seismic structure of the oceanic upper mantle, *Earth Planet. Sci. Lett.*, **282**, 178–189, doi:10.1016/j.epsl.2009.03.014.
- Bhattacharyya, J., G. Masters, and P. M. Shearer (1996), Global lateral variations of shear-wave attenuation in the upper mantle, *J. Geophys. Res.*, **101**, 22,273–22,289.
- Billien, M., J. L  v  que, and J. Trampert (2000), Global maps of Rayleigh wave attenuation for periods between 40 and 150 seconds, *Geophys. Res. Lett.*, **27**, 3619–3622, doi:10.1029/2000GL011389.
- Braun, M. G., G. Hirth, and E. M. Parmentier (2000), The effects of deep damp melting on mantle flow and melt generation beneath mid-ocean ridges, *Earth Planet. Sci. Lett.*, **176**, 339–356, doi:10.1016/S0012-821X(00)00015-7.
- Cammarano, F., S. Goes, P. Vacher, and D. Giardini (2003), Inferring upper mantle temperatures from seismic velocities, *Phys. Earth Planet. Inter.*, **138**, 197–222, doi:10.1016/S0031-9201(03)00156-0.
- Carbotte, S. M., C. Small, and K. Donnelly (2004), The influence of ridge migration on the magmatic segmentation of mid-ocean ridges, *Nature*, **429**, 743–746, doi:10.1038/nature02652.
- Cheadle, M. J., M. T. Elliott, and D. McKenzie (2004), Percolation threshold and permeability of crystallizing igneous rocks: The importance of textural equilibrium, *J. Petrol.*, **32**, 757–760.
- Conder, J. A., D. W. Forsyth, and E. M. Parmentier (2002), Asthenospheric flow and asymmetry of the East Pacific Rise, MELT area, *J. Geophys. Res.*, **107**(B12), 2344, doi:10.1029/2001JB000807.
- Connolly, J. A. D. (2005), Computation of phase equilibria by linear programming: A tool for geodynamic modeling and its application to subduction zone decarbonation, *Earth Planet. Sci. Lett.*, **236**, 524–541, doi:10.1016/j.epsl.2005.04.033.
- Connolly, J. A. D., M. W. Schmidt, G. Solferino, and N. Bagdassarov (2009), Permeability of asthenospheric mantle and melt extraction rates at mid-ocean ridges, *Nature*, **462**, 209–212, doi:10.1038/nature08517.
- Dalton, C. A., and U. H. Faul (2010), The oceanic and cratonic upper mantle: Clues from joint interpretation of global velocity and attenuation models, *Lithos*, **120**, 160–172, doi:10.1016/j.lithos.2010.08.020.
- Dalton, C. A., G. Ekstr  m, and A. Dziewonski (2008), The global attenuation structure of the upper mantle, *J. Geophys. Res.*, **113**, B09303, doi:10.1029/2007JB005429.
- Dalton, C. A., G. Ekstr  m, and A. Dziewonski (2009), Global seismological shear velocity and attenuation: A comparison with experimental observations, *Earth Planet. Sci. Lett.*, **284**, 65–75, doi:10.1016/j.epsl.2009.04.009.

- Dixon, J. E., E. Stolper, and J. R. Delaney (1988), Infrared spectroscopic measurements of CO₂ and H₂O in Juan de Fuca Ridge basaltic glasses, *Earth Planet. Sci. Lett.*, **90**, 87–104, doi:10.1016/0012-821X(88)90114-8.
- Dunn, R. A., and D. W. Forsyth (2003), Imaging the transition between the region of mantle melt generation and the crustal magma chamber beneath the southern East Pacific Rise with short-period Love waves, *J. Geophys. Res.*, **108**(B7), 2352, doi:10.1029/2002JB002217.
- Dziewonski, A., and D. L. Anderson (1981), Preliminary reference Earth model, *Phys. Earth Planet. Inter.*, **25**, 297–356, doi:10.1016/0031-9201(81)90046-7.
- Eggler, D. H. (1976), Does CO₂ cause partial melting in the low-velocity layer of the mantle?, *Geology*, **4**(2), 69–72, doi:10.1130/0091-7613(1976)4<69:DCCPMI>2.0.CO;2.
- Ekström, G., and A. M. Dziewonski (1998), The unique anisotropy of the Pacific upper mantle, *Nature*, **394**, 168–172, doi:10.1038/28148.
- Farla, R. J. M., I. Jackson, J. D. Fitz Gerald, U. H. Faul, and M. E. Zimmerman (2012), Dislocation damping and anisotropic seismic wave attenuation in Earth's upper mantle, *Science*, **336**, 332–335, doi:10.1126/science.1218318.
- Faul, U. H. (2001), Melt retention and segregation beneath mid-ocean ridges, *Nature*, **410**, 920–923, doi:10.1038/35073556.
- Faul, U. H., and I. Jackson (2005), The seismological signature of temperature and grain size variations in the upper mantle, *Earth Planet. Sci. Lett.*, **234**(1–2), 119–134, doi:10.1016/j.epsl.2005.02.008.
- Faul, U. H., J. D. Fitz Gerald, and I. Jackson (2004), Shear wave attenuation and dispersion in melt-bearing olivine polycrystals: 2. Microstructural interpretation and seismological implications, *J. Geophys. Res.*, **109**, B06202, doi:10.1029/2003JB002407.
- Forsyth, D. W., et al. (1998), Imaging the deep seismic structure beneath a mid-ocean ridge: The MELT experiment, *Science*, **280**, 1215–1218, doi:10.1126/science.280.5367.1215.
- Gaherty, J. B., and R. A. Dunn (2007), Evaluating hot spot–ridge interaction in the Atlantic from regional-scale seismic observations, *Geochem. Geophys. Geosyst.*, **8**, Q05006, doi:10.1029/2006GC001533.
- Goes, S., and S. van der Lee (2002), Thermal structure of the North American uppermost mantle inferred from seismic tomography, *J. Geophys. Res.*, **107**(B3), 2050, doi:10.1029/2000JB000049.
- Goes, S., R. Govers, and P. Vacher (2000), Shallow upper mantle temperatures under Europe from *P* and *S* wave tomography, *J. Geophys. Res.*, **105**, 11,153–11,169.
- Goes, S., F. J. Simons, and K. Yoshizawa (2005), Seismic constraints on temperature of the Australian uppermost mantle, *Earth Planet. Sci. Lett.*, **236**, 227–237, doi:10.1016/j.epsl.2005.05.001.
- Gu, Y. J., S. C. Webb, A. Lerner-Lam, and J. B. Gaherty (2005), Upper mantle structure beneath the eastern Pacific Ocean ridges, *J. Geophys. Res.*, **110**, B06305, doi:10.1029/2004JB003381.
- Gung, Y., and B. Romanowicz (2004), Q tomography of the upper mantle using three-component long-period waveforms, *Geophys. J. Int.*, **157**, 813–830, doi:10.1111/j.1365-246X.2004.02265.x.
- Hammond, W. C., and E. D. Humphreys (2000a), Upper mantle seismic wave attenuation: Effects of realistic partial melt distribution, *J. Geophys. Res.*, **105**, 10,987–10,999.
- Hammond, W. C., and E. D. Humphreys (2000b), Upper mantle seismic wave velocity: Effects of realistic partial melt geometries, *J. Geophys. Res.*, **105**, 10,975–10,986.
- Hammond, W. C., and D. R. Toomey (2003), Seismic velocity anisotropy and heterogeneity beneath the Mantle Electromagnetic and Tomography Experiment (MELT) region of the East Pacific Rise from analysis of *P* and *S* body waves, *J. Geophys. Res.*, **108**(B4), 2176, doi:10.1029/2002JB001789.
- Harmon, N., D. W. Forsyth, and D. S. Weeraratne (2009), Thickening of young Pacific lithosphere from high-resolution Rayleigh wave tomography: A test of the conductive cooling mode, *Earth Planet. Sci. Lett.*, **278**, 96–106, doi:10.1016/j.epsl.2008.11.025.
- Harmon, N., D. W. Forsyth, D. S. Weeraratne, Y. Yang, and D. S. Shearer (2011), Mantle heterogeneity and off axis volcanism on young Pacific lithosphere, *Earth Planet. Sci. Lett.*, **311**, 306–315, doi:10.1016/j.epsl.2011.09.038.
- Herzberg, C., P. Ratteron, and J. Zhang (2000), New experimental observations on the anhydrous solidus for peridotite KLB-1, *Geochem. Geophys. Geosyst.*, **1**(11), 1051, doi:10.1029/2000GC000089.
- Herzberg, C., P. D. Asimow, N. Arndt, Y. Niu, C. M. Leshner, J. G. Fitton, M. J. Cheadle, and A. D. Saunders (2007), Temperatures in ambient mantle and plumes: Constraints from basalts, picrites, and komatiites, *Geochem. Geophys. Geosyst.*, **8**, Q02006, doi:10.1029/2006GC001390.
- Hirschmann, M. M. (2010), Partial melt in the oceanic low velocity zone, *Phys. Earth Planet. Inter.*, **179**, 60–71, doi:10.1016/j.pepi.2009.12.003.
- Hirschmann, M. M., P. D. Asimow, M. S. Ghiorso, and E. Stolper (1999), Calculation of peridotite partial melting from thermodynamic models of minerals and melts: III. Controls on isobaric melt production and the effect of water on melt production, *J. Petrol.*, **40**, 831–851, doi:10.1093/ptro/40.5.831.
- Hirschmann, M. M., T. Tenner, C. Abaud, and A. C. Withers (2009), Dehydration melting of nominally anhydrous mantle: The primacy of partitioning, *Phys. Earth Planet. Inter.*, **176**, 54–68, doi:10.1016/j.pepi.2009.04.001.
- Hirth, G., and D. L. Kohlstedt (1996), Water in the oceanic upper mantle: Implications for rheology, melt extraction and the evolution of the lithosphere, *Earth Planet. Sci. Lett.*, **144**, 93–108, doi:10.1016/0012-821X(96)00154-9.
- Hwang, Y. K., J. Ritsema, and S. Goes (2009), Spatial variations of *P* wave attenuation in the mantle beneath North America, *J. Geophys. Res.*, **114**, B06312, doi:10.1029/2008JB006091.
- Hwang, Y. K., J. Ritsema, and S. Goes (2011), Global variation of body-wave attenuation in the upper mantle from teleseismic *P* wave and *S* wave spectra, *Geophys. Res. Lett.*, **38**, L08311, doi:10.1029/2011GL046812.
- Jackson, I., and U. H. Faul (2010), Grain size-sensitive viscoelastic relaxation in olivine: Towards a robust laboratory-based model for seismological application, *Phys. Earth Planet. Inter.*, **183**, 151–163, doi:10.1016/j.pepi.2010.09.005.
- Jackson, I., J. D. Fitz Gerald, U. H. Faul, and B. H. Tan (2002), Grain-size-sensitive seismic wave attenuation in polycrystalline olivine, *J. Geophys. Res.*, **107**(B12), 2360, doi:10.1029/2001JB001225.
- Jha, K., E. M. Parmentier, and J. Phipps Morgan (1994), The role of mantle depletion and melt-retention buoyancy in spreading-center segmentation, *Earth Planet. Sci. Lett.*, **125**, 221–234, doi:10.1016/0012-821X(94)90217-8.
- Karato, S.-I. (1993), Importance of anelasticity in the interpretation of seismic tomography, *Geophys. Res. Lett.*, **20**, 1623–1626, doi:10.1029/93GL01767.
- Karato, S.-I. (2012), On the origin of the asthenosphere, *Earth Planet. Sci. Lett.*, **321**–322, 95–103, doi:10.1016/j.epsl.2012.01.001.
- Karato, S.-I., and H. Jung (1998), Water, partial melting and the origin of the seismic low velocity and high attenuation zone in the upper mantle, *Earth Planet. Sci. Lett.*, **157**(3–4), 193–207, doi:10.1016/S0012-821X(98)00034-X.
- Karato, S., and H. A. Spetzler (1990), Defect microdynamics in minerals and solid-state mechanisms of seismic wave attenuation and velocity dispersion in the mantle, *Rev. Geophys.*, **28**, 399–421, doi:10.1029/RG028i004p00399.
- Katz, R. F. (2010), Porosity-driven convection and asymmetry beneath mid-ocean ridges, *Geochem. Geophys. Geosyst.*, **11**, Q0AC07, doi:10.1029/2010GC003282.
- Katz, R. F., M. Spiegelman, and C. H. Langmuir (2003), A new parameterization of hydrous mantle melting, *Geochem. Geophys. Geosyst.*, **4**(9), 1073, doi:10.1029/2002GC000433.
- Kawakatsu, H., P. Kumar, Y. Takei, M. Shinohara, T. Kanazawa, E. Araki, and K. Suyehiro (2009), Seismic evidence for sharp lithosphere–asthenosphere boundaries of oceanic plates, *Science*, **324**, 499–502.
- Kelley, K. A., T. Plank, S. Newman, E. Stolper, T. L. Grove, S. Parman, and E. H. Hauri (2010), Mantle melting as a function of water content beneath the Mariana Arc, *J. Petrol.*, **51**, 1711–1738, doi:10.1093/ptrology/egq036.
- Kreutzmann, A., H. Schmeling, A. Junge, T. Ruedas, G. Marquart, and I. T. Bjarnason (2004), Temperature and melting of a ridge-centred plume with application to Iceland. Part II: Predictions for electromagnetic and seismic observables, *Geophys. J. Int.*, **159**, 1097–1111, doi:10.1111/j.1365-246X.2004.02397.x.
- Kustowski, B., G. Ekström, and A. Dziewonski (2008), Anisotropic shear-wave velocity structure of the Earth's mantle: A global model, *J. Geophys. Res.*, **113**, B06306, doi:10.1029/2007JB005169.
- Lambert, I. B., and P. J. Wyllie (1968), Stability of hornblende and a model for the low velocity zone, *Nature*, **219**, 1240–1241, doi:10.1038/2191240a0.
- Lekić, V., J. Matas, M. Panning, and B. Romanowicz (2009), Measurement and implications of frequency dependence of attenuation, *Earth Planet. Sci. Lett.*, **282**, 285–293, doi:10.1016/j.epsl.2009.03.030.
- Lundstrom, C. C. (2003), Uranium-series disequilibria in mid-ocean ridge basalts: Observations and models of basalt genesis, *Rev. Mineral. Geochem.*, **52**, 175–214, doi:10.2113/0520175.
- Maggi, A., E. Debayle, K. Priestley, and G. Barruol (2006), Multimode surface waveform tomography of the Pacific Ocean: A closer look at the lithospheric cooling signature, *Geophys. J. Int.*, **166**, 1384–1397, doi:10.1111/j.1365-246X.2006.03037.x.
- Matas, J., and M. S. T. Bukowski (2007), On the anelastic contribution to the temperature dependence of lower mantle seismic velocities, *Earth Planet. Sci. Lett.*, **259**(1–2), 51–65, doi:10.1016/j.epsl.2007.04.028.
- McCarthy, C., and Y. Takei (2011), Anelasticity and viscosity of partially molten rock analogue: Toward seismic detection of small quantities of melt, *Geophys. Res. Lett.*, **38**, L18306, doi:10.1029/2011GL048776.
- McCarthy, C., Y. Takei, and T. Hiraga (2011), Experimental study of attenuation and dispersion over a broad frequency range: 2. The universal

- scaling of polycrystalline materials, *J. Geophys. Res.*, **116**, B09207, doi:10.1029/2011JB008384.
- McKenzie, D. (1984), The generation and compaction of partially molten rock, *J. Petrol.*, **25**, 713–765.
- McKenzie, D., and M. J. Bickle (1988), The volume and composition of melt generated by extension of the lithosphere, *J. Petrol.*, **29**, 625–679.
- McKenzie, D., J. Jackson, and K. Priestley (2005), Thermal structure of oceanic and continental lithosphere, *Earth Planet. Sci. Lett.*, **233**, 337–349, doi:10.1016/j.epsl.2005.02.005.
- Michael, P. J. (1988), The concentration, behavior and storage of H₂O in the suboceanic upper mantle: Implications for mantle metasomatism, *Geochim. Cosmochim. Acta*, **52**, 555–566, doi:10.1016/0016-7037(88)90110-X.
- Michael, P. J. (1995), Regionally distinctive sources of depleted MORB: Evidence from trace elements and H₂O, *Earth Planet. Sci. Lett.*, **131**, 301–320, doi:10.1016/0012-821X(95)00023-6.
- Minster, J. B., and D. L. Anderson (1981), A model of dislocation-controlled rheology for the mantle, *Philos. Trans. R. Soc. London*, **299**, 22,199–22,207.
- Mitchell, B. (1995), Anelastic structure and evolution of the continental-crust and upper-mantle from seismic surface-wave attenuation, *Rev. Geophys.*, **33**, 441–462, doi:10.1029/95RG02074.
- Moresi, L., and V. S. Solomatov (1995), Numerical investigation of 2D convection with extremely large viscosity variations, *Phys. Fluids*, **7**, 2154–2162, doi:10.1063/1.868465.
- Nielsen, T. K., and J. R. Hopper (2004), From rift to drift: Mantle melting during continental breakup, *Geochem. Geophys. Geosyst.*, **5**, Q07003, doi:10.1029/2003GC000662.
- Nishimura, C. E., and D. W. Forsyth (1989), The anisotropic structure of the upper mantle in the Pacific, *Geophys. J. Int.*, **96**, 203–229, doi:10.1111/j.1365-246X.1989.tb04446.x.
- Phipps Morgan, J. (2001), Thermodynamics of pressure release melting of a veined plum pudding mantle, *Geochem. Geophys. Geosyst.*, **2**(4), 1001, doi:10.1029/2000GC000049.
- Priestley, K., and D. McKenzie (2006), The thermal structure of the lithosphere from shear wave velocities, *Earth Planet. Sci. Lett.*, **244**, 285–301, doi:10.1016/j.epsl.2006.01.008.
- Reynard, B., J. D. Bass, and J. Brenizer (2010), High-pressure elastic softening of orthopyroxene and seismic properties of the lithospheric upper mantle, *Geophys. J. Int.*, **181**, 557–566, doi:10.1111/j.1365-246X.2010.04524.x.
- Ritzwoller, M. H., N. M. Shapiro, and S.-J. Zhong (2004), Cooling history of the Pacific lithosphere, *Earth Planet. Sci. Lett.*, **226**, 69–84, doi:10.1016/j.epsl.2004.07.032.
- Robinson, C. J., M. J. Bickle, T. A. Minshull, R. S. White, and A. R. L. Nichols (2001), Low degree melting under the Southwest Indian Ridge: The roles of mantle temperature, conductive cooling and wet melting, *Earth Planet. Sci. Lett.*, **188**, 383–398, doi:10.1016/S0012-821X(01)00329-6.
- Röhm, A. H. E., R. K. Snieder, S. Goes, and J. Trampert (2000), Thermal structure of continental upper mantle inferred from *S* wave velocity and surface heat flow, *Earth Planet. Sci. Lett.*, **181**, 395–407, doi:10.1016/S0012-821X(00)00209-0.
- Rubin, K. H., I. Van der Zander, M. C. Smith, and E. C. Bergmanis (2005), Minimum speed limit for ocean ridge magmatism from ²¹⁰Pb–²²⁶Ra–²³⁰Th disequilibria, *Nature*, **437**, 534–538, doi:10.1038/nature03993.
- Rychert, C. A., and P. M. Shearer (2009), A global view of the lithosphere–asthenosphere boundary, *Science*, **324**, 495–498, doi:10.1126/science.1169754.
- Saito, M. (1988), DISPER80: A subroutine package for the calculation of seismic normal-mode solutions, in *Seismological Algorithms: Computational Methods and Computer Programs*, edited by D. J. Doornbos, pp. 293–319, Academic, San Diego, Calif.
- Scheirer, D. S., K. C. Macdonald, D. W. Forsyth, S. P. Miller, D. J. Wright, M. H. Cormier, and C. M. Weiland (1996), A map series of the Southern East Pacific Rise and its flanks, 15°S to 19°S, *Mar. Geophys. Res.*, **18**, 1–12, doi:10.1007/BF00286201.
- Scott, D. R. (1992), Small-scale convection and mantle melting beneath mid-ocean ridges, in *Mantle Flow and Melt Generation at Mid-Ocean Ridges*, *Geophys. Monogr. Ser.*, vol. 71, edited by J. Phipps Morgan, D. K. Blackman, and J. M. Sinton, pp. 327–352, AGU, Washington, D. C., doi:10.1029/GM071p0327.
- Scott, D. R., and D. J. Stevenson (1989), A self-consistent model of melting, magma migration and buoyancy-driven circulation beneath mid-ocean ridges, *J. Geophys. Res.*, **94**(B3), 2973–2988, doi:10.1029/JB094iB03p02973.
- Shapiro, N. M., and M. H. Ritzwoller (2002), Monte-Carlo inversion for a global shear-velocity model of the crust and upper mantle, *Geophys. J. Int.*, **151**, 88–105, doi:10.1046/j.1365-246X.2002.01742.x.
- Shapiro, N. M., and M. H. Ritzwoller (2004a), Inferring surface heat flux distributions guided by a global seismic model: Particular application to Antarctica, *Earth Planet. Sci. Lett.*, **223**, 213–224, doi:10.1016/j.epsl.2004.04.011.
- Shapiro, N. M., and M. H. Ritzwoller (2004b), Thermodynamic constraints on seismic inversions, *Geophys. J. Int.*, **157**, 1175–1188, doi:10.1111/j.1365-246X.2004.02254.x.
- Sheehan, A. F., and S. C. Solomon (1992), Differential shear wave attenuation and its lateral variation in the North Atlantic region, *J. Geophys. Res.*, **97**(B11), 15,339–15,350.
- Sparks, D. W., and E. M. Parmentier (1991), Melt extraction from the mantle beneath spreading centers, *Earth Planet. Sci. Lett.*, **105**, 368–377, doi:10.1016/0012-821X(91)90178-K.
- Spiegelman, M., and D. McKenzie (1987), Simple 2-D models for melt extraction at mid-ocean ridges and island arcs, *Earth Planet. Sci. Lett.*, **83**, 137–152.
- Stixrude, L., and C. Lithgow-Bertelloni (2005), Mineralogy and elasticity of the oceanic upper mantle: Origin of the low-velocity zone, *J. Geophys. Res.*, **110**, B03204, doi:10.1029/2004JB002965.
- Stracke, A., B. Bourdon, and D. McKenzie (2006), Melt extraction in the Earth's mantle: Constraints from U-Th-Pa-Ra studies in oceanic basalts, *Earth Planet. Sci. Lett.*, **244**, 97–112, doi:10.1016/j.epsl.2006.01.057.
- Takei, Y. (2002), Effect of pore geometry on *V_p/V_s*: From equilibrium geometry to crack, *J. Geophys. Res.*, **107**(B2), 2043, doi:10.1029/2001JB000522.
- Toomey, D. R., W. S. D. Wilcock, J. A. Conder, D. W. Forsyth, J. W. Blundy, E. M. Parmentier, and W. C. Hammond (2002), Asymmetric mantle dynamics in the MELT region of the East Pacific Rise, *Earth Planet. Sci. Lett.*, **200**, 287–295, doi:10.1016/S0012-821X(02)00655-6.
- van Wijk, J., J. Van Hunen, and S. Goes (2008), Small-scale convection during continental rifting: Evidence from the Rio Grande rift, *Geology*, **36**(7), 575–578, doi:10.1130/G24691A.1.
- Wang, Y., D. W. Forsyth, and B. Savage (2009), Convective upwelling in the mantle beneath the Gulf of California, *Nature*, **462**, 499–501, doi:10.1038/nature08552.
- Wark, D. A., and E. B. Watson (1998), Grain-scale permeabilities of texturally equilibrated monomineralic rocks, *Earth Planet. Sci. Lett.*, **164**, 591–605, doi:10.1016/S0012-821X(98)00252-0.
- Webb, S. C., and D. W. Forsyth (1998), Structure of the upper mantle under the EPR from waveform inversion of regional events, *Science*, **280**, 1227–1229, doi:10.1126/science.280.5367.1227.
- Weeraratne, D. S., D. W. Forsyth, Y. Yang, and S. C. Webb (2007), Rayleigh wave tomography beneath intraplate volcanic ridges in the South Pacific, *J. Geophys. Res.*, **112**, B06303, doi:10.1029/2006JB004403.
- Wessel, P., and W. H. F. Smith (1998), New, improved version of Generic Mapping Tools released, *Eos Trans. AGU*, **79**(47), 579, doi:10.1029/98EO00426.
- Wyllie, P. J., and W.-L. Huang (1975), Peridotite, kimberlite, and carbonate explained in the system CaO-MgO-SiO₂-CO₂, *Geology*, **3**(11), 621–624, doi:10.1130/0091-7613(1975)3<621:PKACEI>2.0.CO;2.
- Xu, W., C. Lithgow-Bertelloni, L. Stixrude, and J. Ritsema (2008), The effect of bulk composition and temperature on mantle seismic structure, *Earth Planet. Sci. Lett.*, **275**, 70–79, doi:10.1016/j.epsl.2008.08.012.
- Yang, Y., D. W. Forsyth, and D. S. Weeraratne (2007), Seismic attenuation near the East Pacific Rise and the origin of the low-velocity zone, *Earth Planet. Sci. Lett.*, **258**, 260–268, doi:10.1016/j.epsl.2007.03.040.
- Zaroli, C., E. Debayle, and M. Sambridge (2010), Frequency-dependent effects on global *S*-wave traveltimes: Wavefront-healing, scattering and attenuation, *Geophys. J. Int.*, **182**, 1025–1042, doi:10.1111/j.1365-246X.2010.04667.x.
- Zhu, W., G. A. Gaetani, F. Fusseis, L. Montési, and F. De Carlo (2011), Microtomography of partially molten rocks: Three-dimensional melt distribution in mantle peridotite, *Science*, **332**, 88–91, doi:10.1126/science.1202221.